SPH method for long-time simulations of sloshing flows in LNG tanks

C. Pilloton[a], A. Bardazzi[a,b], A. Colagrossi[a], S. Marrone[a]

[a]*CNR - INM, Institute of Marine Engineering, Via di Vallerano 139, 00128, Rome, Italy*
[b]*Department of Engineering, University of Campania "Luigi Vanvitelli", Via Roma, 29, 81031 Aversa, Italy;*

Abstract

The present work is dedicated to the numerical investigation of sloshing flows inside a ship LNG fuel tank. Long time simulations, involving 3-hours real–time duration with realistic severe sea-state forcing, have been performed using a parallel CFD solver running for several weeks on a dedicated cluster. The numerical model adopted is the Smoothed Particle Hydrodynamics model (SPH). This model has been chosen for its Lagrangian approach and for the intrinsic properties of mass and momenta conservation which makes it well adapted for the simulation of violent free-surface flows. The adopted SPH method relies on a Riemann Solver for the calculation of the particle interactions which increases the stability of the scheme and allows for accurate predictions of the pressure during water impact stages. Three different filling height conditions are considered. For all of them energetic sloshing flows are induced with the occurrence of several water impact events. The latter are focused on specific zones of the tank depending on the considered filling height. For some conditions the SPH pressure predictions are compared with experimental ones. A critical discussion of these predictions is performed, highlighting the cases in which the numerical solver is able to provide good local pressure estimations.

Keywords: Sloshing Flows, LNG ship, Water Impact, Slamming loads, Smoothed Particle Hydrodynamics, SPH

1. Introduction

Because of the commitment of nations to reduce noxious emissions of standard fuels,notably NOx and SOx oxide. the consumption of the Liquefied Natural Gas (LNG) fuel has largely increased during the recent years. In the period from 2018 to 2020, the market experienced a record commissioning of LNG carriers: 139 tankers entered service. As a result, more than 600 LNG tankers were operating on the global market in early 2021. In order to increase the demand of LNG, larger LNG carriers start to be designed and planned. LNG storage and transportation are critical issues in the design and safety aspects of those carriers. In particular, the Cargo Containment System (CCS), which has the task of keeping the liquid at a low temperature (-165^o C), is a fundamental component. The CCS is a composite structure of metal membrane, laminated insulation in polyurethane foam and plywood and its strength can be characterized as the maximum load that the system can bear before it fails. The loads acting on the insulation system

*Corresponding author
Email address: andrea.bardazzi@unicampania.it (A. Bardazzi)

are due to the liquid sloshing which can induce slamming loads characterized by an impulsive loading process, *i.e.* the loads are localized in space and time. The preservation of the CSS integrity on the new generation LNG ships is one of the primary focus that challenged shipyards engineers (for an in-depth discussion see *e.g* Kuo et al. (2009)). Although performances of the new LNG carriers is excellent, insulation tanks can incur damages due to LNG sloshing impacts under both high-fill and partial-fill conditions, as happened in the past and documented in Jean and Petit (1998).

Since the 1980s industries have supported studies on sloshing flows. In this field, mainly small-scale experiments have been adopted due to the stochastic character of sloshing problems and the related complex flow features (see *e.g* Diebold and Baudin (2014); Loysel et al. (2012, 2013); Wei et al. (2014)). These aspects have always restricted the adoption of numerical methods to a deterministic-based approach where only few periods of oscillation were considered. Nowadays, thanks to the advancement in computing capabilities, sloshing simulations can be performed for long-time duration (beyond 1,000 cycles) moving the analysis toward a statistical approach as required by modern industrial designs.

The objective of the present research activity is the achievement of sloshing simulations inside ship LNG tanks characterized by 3-hours real–time duration with realistic severe sea-state forcing. To this aim the tank model of Hyundai Heavy has been adopted and the experimental campaigns performed at Seoul National University (see Ahn (2019) and further studies in Kim et al. (2017); Ahn et al. (2019); Ahn and Kim (2021)) has been taken as reference. The numerical model adopted is an enhanced Smoothed Particle Hydrodynamics (SPH) model described in section 4.1. It is important to stress some aspects related to this specific problem:

- There is absence of literature for this kind of application: to the authors' knowledge there are no publications on the application of Navier-Stokes solvers for simulating sloshing flows with such a long time duration.
- The CPU requirements are very large, the maximum number of particles adopted is 400,000 particles with about 10 Millions of time iterations.
- The temporal resolution, which depends on the the spatial discretization adopted, allows a numerical time sampling rate of 9 KHz, which is of the same order of the experimental sampling rate of 20 KHz.
- Validations against experiments require a statistical analysis and the data processing procedures of the SPH results have been treated consistently with the experimental time signals.

The paper is organized as follows: in section 2 the problem geometry is described and the experimental conditions are provided; in section 3 the governing equations are briefly discussed. In section 4 the numerical model adopted is described along with the numerical setup; on the base of preliminary 2D simulations some key aspects of the numerical simulation are discussed such as the relevance of the weakly-compressible assumption; in section 5 the numerical results are discussed for the different test conditions considered. The pressure peaks recorded are extracted through a Peak Over Threshold (POT) procedure and a brief statistical analysis is given for some selected probes DNV (2006); in section 6 a statistical analysis of the outcomes of the numerical simulations is provided and the global outputs obtained over all the 40 probes for each case is described through synthetic indicators; finally, conclusions wrap up the paper.

2. Problem description

The problem consists in a LNG tank subjected to an imposed motion in all the 6 degrees of freedom (6-DOF). The tank is partially filled with water and different filling height conditions are considered. The tank geometry is reported in figure 1 where the pivot used to enforce the given 6-DOF motion is also depicted. The total height of the tank is 20.77m and the three different filling conditions studied are:

- 30% Small water filling height case, labeled as **SW** ,
- 60% Intermediate water filling height case, labeled as **IW** ,
- 90% Deep water filling height case, labeled as **DW** .

For each of these conditions, different 6-DOF time histories were provided. A realistic law of motion is considered. To this aim the motions of a ship travelling in the North Atlantic route (significant wave height envelope fitted to 40 year return period) are taken as reference. The motion time history is generated using a Pierson-Moskowitz spectrum with significant wave height 11.1 m and zero crossing period 9.5 sec in a heading angle condition of 90°. A 3D solver based on potential flow theory was used to calculate the ship motions excited by the selected sea spectrum. The adopted commercial software is able to solve the seakeeping-sloshing coupled analysis in forward motion in a simplified way (for more details see *e.g.* Malenica et al. (2009)). Under the above sea conditions, large tank motions are induced especially in the vertical direction (heave motion).

Figure 2 depicts a time window of 1000 seconds for the heave, sway and roll motions imposed to the tank in the **DW** case. These three degrees of motion are the most excited (surge, pitch and yaw motions are much smaller), in particular the heave motion presents a maximum amplitude of about 18 meters, while for the horizontal motion the oscillations are in the range between [-5, +5] meters. Concerning the roll motion this is always confined in the interval [-2, +2] degrees. In the three time histories the first 20 minutes are considered as a warm-up scenario and therefore the pressure measurements

LNG fuel tank dimension for One-row tank

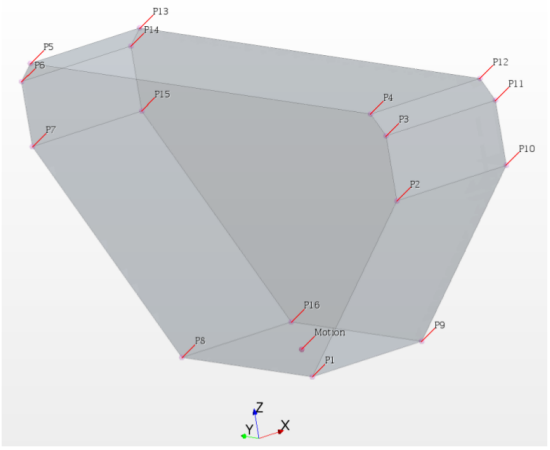

	X [m]	Y [m]	Z [m]
P1	0	-8.031	5.305
P2	0	-22.44	19.714
P3	0	-22.44	24.556
P4	0	-20.951	26.045
P5	0	20.951	26.045
P6	0	22.44	24.556
P7	0	22.44	19.714
P8	0	8.031	5.305
P9	9.86	-8.031	5.305
P10	9.86	-22.44	19.714
P11	9.86	-22.44	24.556
P12	9.86	-20.951	26.045
P13	9.86	20.951	26.045
P14	9.86	22.44	24.556
P15	9.86	22.44	19.714
P16	9.86	8.031	5.305

	X [m]	Y [m]	Z [m]
Motion	4.93	0	5.305

Figure 1: LNG tank geometry in real scale with the coordinates of the different vertices and the position of the Pivot for the constrained motion.

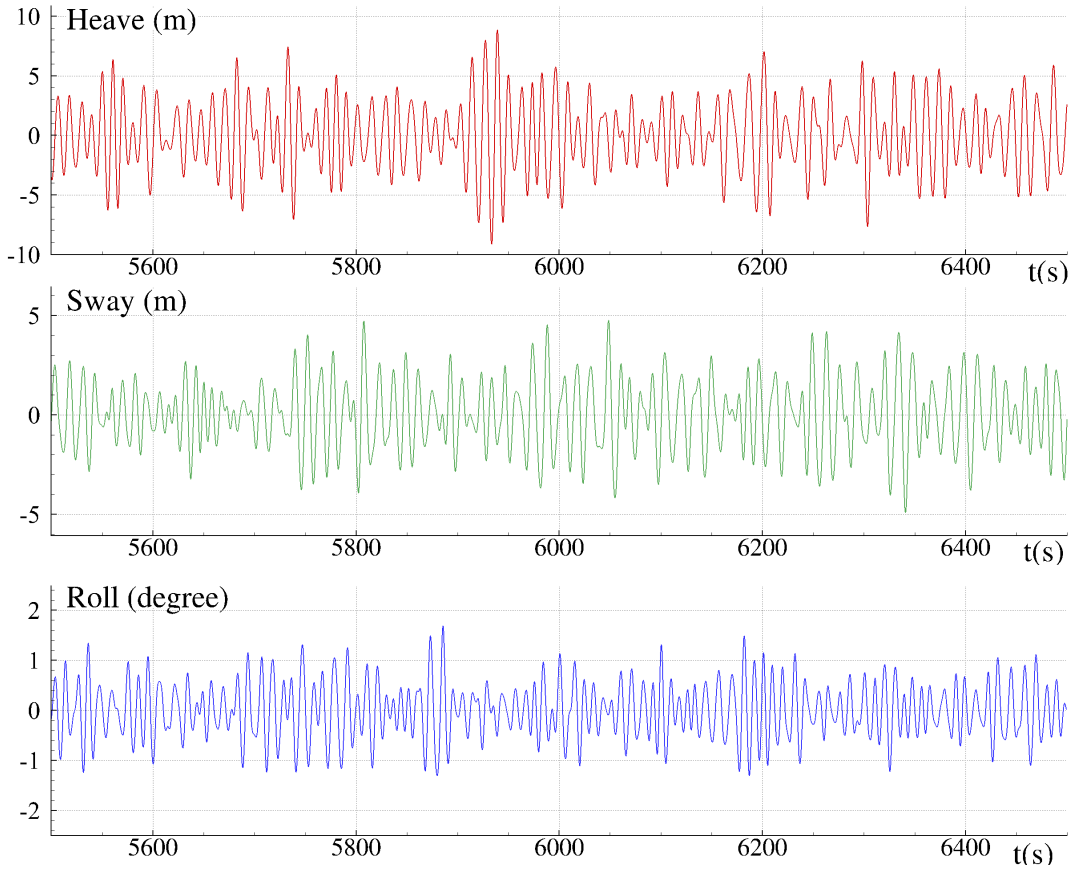

Figure 2: Time window of 1000 seconds of the time histories (real scale) for the heave (top), Sway (middle) and Roll (bottom) motions imposed on the tank for the DW case.

in the simulation started from 1,000 sec and ended at 11,800 sec corresponding to 3 hours of simulation.

The experimental model scale is $\lambda = 1 : 50$ and the SPH simulations are performed at the same scale. However, the quantities referred to SPH are reported in the article scaled to the real size by respecting the Froude scaling (when not otherwise specified). In fact, as shown in, *e.g.*, Moirod et al. (2011); Kim et al. (2017) the main flow features are mostly driven by the Froude number. The role of the gaseous phase can be relevant when local pressure peaks are of interest (see Lugni et al. (2010, 2006)) and other scaling laws should be considered Abrahamsen and Faltinsen (2013). However, since in the SPH simulations the sole liquid phase is considered, only the Froude number is here addressed.

In the adopted SPH model a weakly-compressible approach is used and a Mach number is set. In sections 4.1 and 4.4 the role of this parameter is discussed. Furthermore, a Large Eddy Simulations model is implemented and the sub-grid vortical structures are modeled with a classical Smagorinsky law (see *e.g.* Di Mascio et al. (2017)). As far as wall boundary conditions are concerned, a very high resolution is needed to resolve the boundary layer because the Reynolds number is very high. However, since a uniform spatial resolution is adopted in our simulation, we chose to not solve the boundary layer (which is expected to play a minor role) and, thus, a free–slip condition is imposed at the tank walls.

In section 4.6 we firstly present the analysis performed on 2D preliminary tests. Thanks to the latter we showed that the size of the particles and the time step adopted in 3D are small enough to guarantee a good pressure evaluation during impact events.

Arrangement of pressure sensors

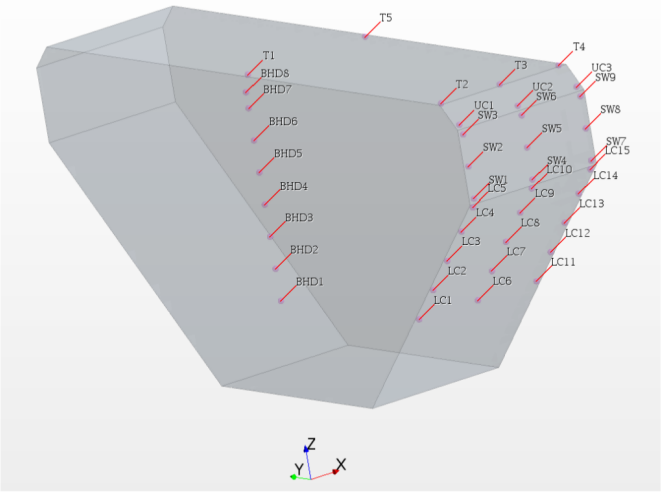

Figure 3: Sketches of the tank geometry with labels and positions of the different pressure probes.

As for the 3D study, some preliminary trial simulations on the three filling-heights have been conducted before running the actual simulations in order to verify the parameter choice, the tank motion and the CPU costs. Figure 3 reports the labels and positions of the different pressure probes used in the experiments as well as in the SPH simulations. For all the three test conditions some flow features related to critical impact events have been considered in section 5.

3. Governing equations

The governing equations adopted in this work are the Navier-Stokes equations (NSE) for a single-phase weakly compressible fluid. Since the Reynolds number of the flow is quite high, a sub-scale grid model has been adopted. The equations solved, written in a Lagrangian formalism are:

$$\begin{cases} \dfrac{D\rho}{Dt} &= -\rho\,\nabla\cdot\mathbf{u} \\ \rho\dfrac{D\mathbf{u}}{Dt} &= -\nabla p + \rho\,\mathbf{g} + (\mu+\mu_T)\nabla^2\mathbf{u} \\ \dfrac{D\mathbf{r}}{Dt} &= \mathbf{u}\,, \qquad p = f(\rho) \end{cases} \tag{1}$$

where D/Dt represents the Lagrangian derivative, while $\mathbf{r}$, $\mathbf{u}$, p and ρ are, respectively, the position of a generic material point, its velocity, pressure and density; and $\mathbf{g}$ represents gravitational acceleration. Regarding the viscous term in the momentum equation μ is the fluid viscosity while μ_T indicates the local turbulent viscosity.

Moreover, the fluid is assumed to be barotropic and the following functional dependence between ρ and p is adopted:

$$p = c_0^2\,(\rho - \rho_0) \tag{2}$$

where ρ_0 is the density of the liquid at the free surface and c_0 is the speed of sound. The weakly-compressible regime implies the following requirement:

$$c_0 \geq \max\left(10U_{max}\,,\,10\sqrt{\frac{(\Delta p)_{max}}{\rho}}\right) \tag{3}$$

where U_{max} and $(\Delta p)_{max}$ respectively are the maximum fluid speed and the maximum pressure variation expected (with respect to the zero pressure free-surface level) in the fluid domain (see Marrone et al. (2016)). For numerical purposes, in order to avoid too small time steps, in the simulations c_0 is chosen smaller than its physical counterpart. Constraint (3) however, has to be respected to guarantee the weakly-compressible regime and this condition has to be verified throughout the simulations.

For the present study, the proper identification of c_0 is crucial, as it will be discussed in the following sections. Considering the Mach number $\mathrm{Ma} = U_{max}/c_0$, the constraint $\mathrm{Ma} < 0.1$ is taken into account to make compressibility effects negligible (i.e. density variations smaller than 1%). However, during violent impact events (i.e., flat impacts) the acoustic pressure $p = \rho\, u\, c_0$ can be reached, and in this case the pressure peak intensity becomes proportional to $1/\mathrm{Ma}$. On the other hand, in such a condition an incompressible constraint can induce singularities on the pressure field. This is linked to the fact that for this kind of impacts the presence of the air phase is generally crucial and the single-phase approach can lead to incorrect pressure evaluations under the incompressible/weakly-compressible hypothesis.

Being aware of these limits for a single-phase model, the results obtained in this work have been critically revised considering a possible Mach dependency. For a more in-depth discussion on this topic see also Marrone et al. (2015, 2016); Meringolo et al. (2017).

4. Numerical Model

Violent sloshing flows can be simulated using different numerical methods. In the recent years Finite Volume Methods coupled with Volume-of-Fluids algorithm have been extensively used for simulating such kind of flows (see for example Lee et al. (2007); Li et al. (2014); Elahi et al. (2015); Lyu et al. (2017); Malan et al. (2021); Gómez-Goñi et al. (2013)). Beside mesh-based solver also Particle Methods like the Smoothed Particle Hydrodynamics (SPH) models have been proved to be powerful numerical solvers for tackling violent sloshing flows. SPH models are Lagrangian meshless method which were developed in the seventies to solve astrophysics problems (see *e.g.* Monaghan (1992)) and because its flexibility it quickly spread over into different disciplines (see *e.g.* Monaghan (2012); Shadloo et al. (2016), including free surface flows, as discussed *e.g.* in the review articles by Violeau and Rogers (2016). Both compressible and incompressible formulations of SPH can be found in the literature. The interested reader can find further insights also in the review article by Luo et al. (2021).

Regarding SPH simulations of sloshing flows, during recent years a thorough validation has been carried out (see *e.g.* Green and Peiró (2018); Cao et al. (2014); Bouscasse et al. (2014a,b, 2013); Shao et al. (2012); Delorme et al. (2009))

The theoretical scheme underlying the SPH model is here briefly summarized. The SPH model is based on the interpolation of a generic flow field f through a convolution integral with a kernel function W (generally a bell-shaped function) over its compact support Ω:

$$\langle f\rangle(\boldsymbol{r}) \;=\; \int_{\Omega} f(\boldsymbol{r}')\, W(\boldsymbol{r}' - \boldsymbol{r}; h)\, dV' \tag{4}$$

The parameter h is the smoothing length which is proportional to the radius of the kernel support. As kernel function a Wendland C2 kernel with a support of radius equal to $2h$ is used in the present SPH scheme.

The fluid domain is discretized into a finite number of particles representing elementary fluid volumes, each with its own local mass m_i and other physical properties. At the discrete level a generic field f evaluated at the position r_i of the i-th particle is approximated through a convolution sum. Equation (4) thus becomes:

$$\langle f \rangle(\boldsymbol{r}_i) \;=\; \sum_j f(\boldsymbol{r}_j)\, W(\boldsymbol{r}_i - \boldsymbol{r}_j; h)\, V_j \tag{5}$$

where V_j is the volume of the j-th particle. Hence any function or its gradient can be interpolated in total absence of connectivity.

The fluid particles are initially positioned using the algorithm described in Colagrossi et al. (2012). Thanks to this procedure, at the initial instant all particles have approximately the same volume, namely V_0, which is equal to the fluid domain volume divided by the number of fluid particles. Consistently, the particle mean spacing is denoted by $\Delta r = V_0^{1/3}$. The average number of particles in the kernel support is set by choosing the ratio $h/\Delta r$. Along with the volume distribution, the initial pressure and the velocity fields are prescribed as well. The initial density distribution $\rho_i(t_0)$ is evaluated by means of the state equation and the particle masses are computed through the equation $m_i = \rho_i(t_0)\, V_0$.

4.1. The Riemann-SPH scheme

In the present work a Riemann-based variant of the classical SPH scheme is adopted. This specific scheme has been adopted for the following reasons:

- the high accuracy in the prediction of pressure liquid impacts (see *e.g.* Marrone et al. (2015, 2017));
- the high robustness of the scheme which helps handling long-time simulations;
- the good volume conservation properties when simulating long-time violent free-surface flows, while for other SPH schemes, like the popular δ^+-SPH schemes, special treatments are needed as discussed recently in Lyu and Sun (2022);
- the treatment of wall boundary condition: within the Riemann-SPH model the new developments described in Chiron et al. (2019) were implemented. The latter is based on a boundary integral approach based on a cutface process for calculating the particle–wall interactions on geometries of arbitrary shapes.

In the specific, the adopted Riemann-SPH scheme is the one proposed by Parshikov and Medin (2002), characterized by zero mass fluxes and resulting in the following discrete equations:

$$\begin{cases} \dfrac{D\,V_i}{Dt} &= 2V_i \displaystyle\sum_j (\boldsymbol{u}_E - \boldsymbol{u}_i)\cdot \nabla W_{ij}\, V_j \\ \dfrac{D\,m_i}{Dt} &= 0 \\ \dfrac{D\,(m_i \boldsymbol{u}_i)}{Dt} &= -V_i \displaystyle\sum_j 2P_E\, \nabla W_{ij}\, V_j \;+\; m_i \boldsymbol{g} \;+\; \boldsymbol{F}_i^v\, V_i \\ \dfrac{D\boldsymbol{r}_i}{Dt} &= \boldsymbol{u}_i, \qquad \rho_i(t) = \dfrac{m_i}{V_i(t)}\,, \qquad p_i \;=\; c_0^2\,(\rho_i - \rho_0) \end{cases} \tag{6}$$

where $\boldsymbol{u}_E$ and P_E are the solutions of the Riemann problem at the interface $\boldsymbol{r}_{ij} = (\boldsymbol{r}_i + \boldsymbol{r}_j)/2$, between particles i and j while $\boldsymbol{F}_i^v$ are the viscous forces acting on the particle i. A MUSCL (Monotone Upstream Scheme for Conservation Laws) procedure is used to increase the order of this Total Variation Diminishing (TVD) scheme. Thanks to the introduction of Riemann-solvers the fluxes between particles are upwind oriented and the resulting scheme is more stable.

4.2. Viscous forces modelling

The viscous forces $\boldsymbol{F}^v$ in equation (6) are expressed as:

$$\begin{cases} \boldsymbol{F}_i^v \;:=\; K \sum_j (\mu \,+\, \mu_{ij}^T)\, \pi_{ij}\, \nabla_i W_{ij}\, V_j\,, & K := 2(n+2)\,, \\ \pi_{ij} \;:=\; \dfrac{\boldsymbol{u}_{ij}\cdot \boldsymbol{r}_{ij}}{\|\boldsymbol{r}_{ji}\|^2}\,, \qquad \mu_{ij}^T := 2\,\dfrac{\mu_i^T\,\mu_j^T}{\mu_i^T \,+\, \mu_j^T}\,, & \mu_i^T \;:=\; \rho_0\,(C_S\; l)^2\,\|\mathbb{D}_i\| \end{cases} \tag{7}$$

where n is the number of spatial dimensions and C_S is the so called Smagorinsky constant set equal to 0.18 (see Smagorinsky (1963)). $\mathbb{D}_i$ is the rate of strain tensor and $\|\mathbb{D}\|$ is a rescaled Frobenius norm, namely $\|\mathbb{D}\| = \sqrt{2\mathbb{D} : \mathbb{D}}$. The viscous term (7) contains both the effect of the fluid viscosity μ as well as the one related to the local turbulent viscosity μ_i^T (for details see Di Mascio et al. (2017)).

4.3. The adopted Software and Hardware

Starting from 2013 CNR-INM participated in building a consortium with the Ecole Centrale de Nantes (ECN) and a Company called NextFlow-Software for developing an industrial SPH code named SPH-Flow. The SPH-Flow solver is very well adapted to HPC, having a high parallel scalability when running on several computational nodes. Scalability up to several thousands of cores have been proven on Tier-0 machines of the PRACE European research infrastructure (for more details see Oger et al. (2016), Maruzewski et al. (2010)).

In order to perform the three long-time 3D simulations for the cases **SW**, **IW** and **DW** some ad-hoc computing blades have been used. The characteristic of the three blades are:

- BLADE N° 1: 64 cores AMD Opteron(tm) Processor 6376, 2.30GHz
- BLADE N° 2: 64 cores Intel(R) Xeon(R) CPU E5-2698 v3, 2.30GHz
- BLADE N° 3: 64 cores Intel(R) Xeon(R) CPU E5-2698 v3, 2.30GHz

Since the blade N° 1 has lower CPU performance, it is dedicated to the **SW** case; this case indeed involves a lower number of particles with respect to the other two cases, **IW** and **DW**, as explained in the next section 4.4. The blade N° 1 has been also used to perform the preliminary 2D analysis.

The SPH-flow solver has been tested on those new blades by evaluating the CPU costs per iteration and per particle for a single computing core in order to get a prediction of the maximum time and spatial resolutions to be adopted for the three simulations. The results of these preliminary tests on the software performance is reported in table 1; those results are used in the next sections to fix the parameters for the 3D simulations. The last column of table 1 shows the CPU-efficiency defined as the time needed to the SPH-flow software to perform one iteration divided by the number of particles presented in the domain and multiplied by the number of cores used. This number allows to get a prediction of the CPU costs and, therefore, to set the maximum number of particles and the maximum number of time iterations for the given computational resources. The CPU-efficiency depends:

- on the ratio $h/\Delta r$ or, in other words, on the number of particle neighbors;
- on the characteristics of the specific CPU adopted;
- on the peculiarities of the simulation which may influence the parallelization efficiency (e.g. presence of boundaries, extension of the domain).

Blade N°	N° of cores	$N_{particles}$	$h/\Delta r$	N° of Neighbors	CPU-efficiency (seconds $\times 10^{-6}$)
1	60	370,000	1.05	39	260
2	60	400,000	1.05	39	124
3	60	480,000	1.1	45	156

Table 1: Evaluation of the CPU-factor. The CPU-factor is the time needed to the SPH-flow software to perform one iteration divided by the number of particles presented in the domain and multiplied by the number of cores used.

4.4. Set-up of the simulation parameters

In order to set-up the parameters for the 3D simulations we need to specify the time and the space discretizations for the available CPU resources. The system (6) is integrated in time by using a fourth-order Runge-Kutta scheme. The time step is obtained as:

$$\Delta t \leq CFL \left(\frac{\Delta r}{c_0}\right)\left(\frac{h}{\Delta r}\right),$$

where the Courant-Friedrichs-Lewy constant is $CFL = 0.6$ for a Wendland C2 Kernel. To ensure the weakly-compressibility, the sound speed has been chosen to satisfy the requirement (3).

For the case **SW** the maximum velocity field expected in the tank can be estimated as $U_{max} = \sqrt{gH}$ being H the filling height, and the speed of sound is therefore set as $c_0 \geq 10\sqrt{gH}$. For the case **DW** the p_{max} pressure can be estimated with the maximum hydrostatic pressure $p_{max} = \rho g H$, and therefore the speed of sound is again $c_0 \geq 10\sqrt{gH}$. The above estimation implies that for the **DW** case a larger speed of sound is needed, $c_0 = 140$ m/s. Furthermore, the **DW** case has a larger fluid domain to be discretized. This means that we cannot use the same spatial discretization for the **SW** and the **DW** cases, if we want to use the computing blades in an efficient way. Even if the speeds of sound for the cases **SW** and **IW** can be set in principle equal to, respectively, $c_0 = 80$ and 110 m/s, we prefer to use higher values, specifically c_0 =120 and 140 m/s, since we expect for these cases slamming loads of the same order of magnitude as in the case **DW** . Using the above information and the CPU-efficiency evaluated in the previous section, the parameters for the 3D simulations can be set and the total CPU costs can be estimated (see table 2). In figure 4 the initial conditions adopted for the three test cases are depicted.

From table 2 it is possible to see that the **IW** case, which runs on the computing blade N°2, will complete the simulation much before the blade N°1. For this reason when the **IW** case was completed we moved the **SW** case from the blade N°1, which has lower CPU performance with respect to the other two, to the blade N°2. As a consequence, in order to balance the CPU load on blade N°3 a larger ratio $h/\Delta r$ has been chosen for the **DW** case.

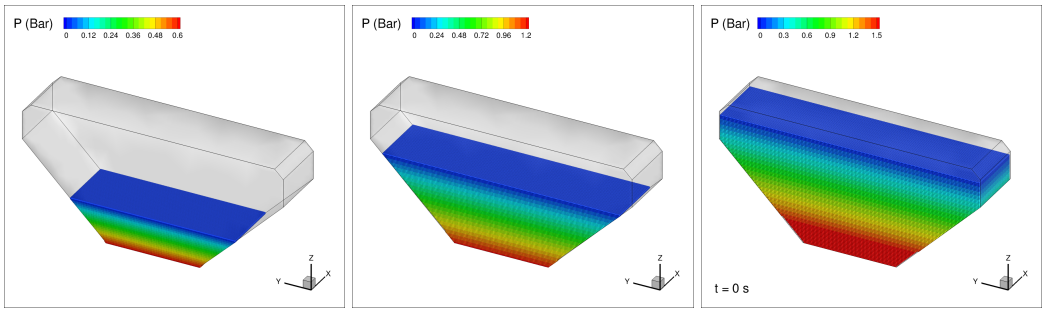

Figure 4: From left to right: particle configurations for the test cases **SW** , **IW** and **DW** .

	H(m)	c_0(m/s)	$H/\Delta r$	N_{part}	Δt (ms)	$N_{iterations}$ (millions)	CPU cost (days)
SW	6.22	120	40	370,000	0.817	14	269
IW	12.44	140	60	400,000	0.933	12.6	122
DW	18.66	140	80	480,000	1.10	10.7	156

Table 2: Parameters used for the 3D SPH simulations.

4.5. Effects and limits of the SPH compressibility during violent impacts

Since in this research investigation the sloshing simulations are characterized by large motions and violent impact events, the estimation on the maximum velocity and pressure values, used in the previous section to set c_0, can be locally overpassed. For this reason a preliminary 2D simulation have been conducted to evaluate the maximum velocity of the fluid during the impact stages. For example in figure 5 the intensity of the velocity field in the tank frame of reference is shown. The fluid velocity just before the impact is about 15 m/s which is just 16% greater than the one predicted in the previous section. It is important to note that the fluid velocity can be even higher than 15 m/s but only for very local fluid portions, like single drops generated by the fragmentation of water jets.

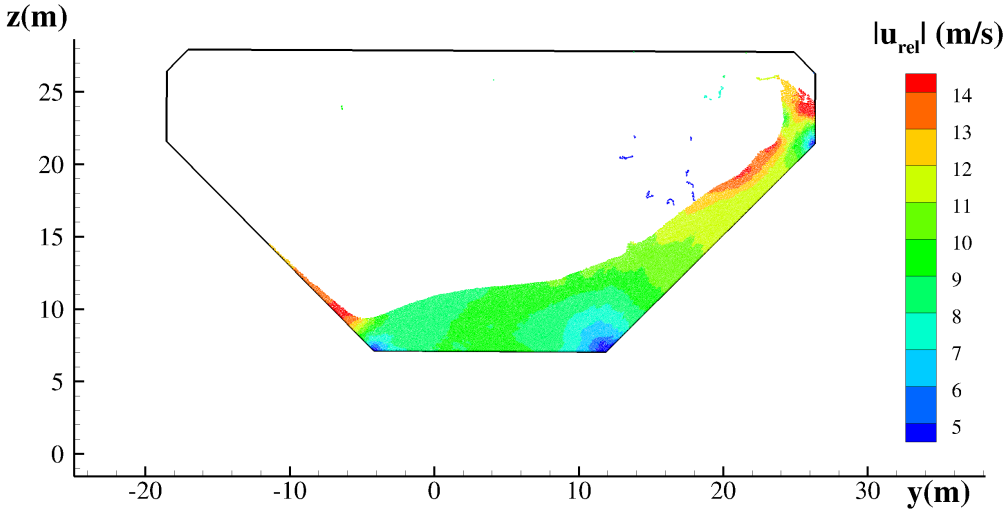

Figure 5: **SW** case: SPH 2D preliminary analysis. Maximum velocity in the tank frame of reference.

A correct setting of the magnitude of the fluid velocity is necessary but not sufficient to ensure that compressible effects are negligible. Indeed, also the pressure has to be taken into account. During impact stages, depending on the water jet geometry, the water-hammer pressure can be reached because of the absence of the air phase. This pressure is

	c_0 (m/s)	U_{max} 2D SPH	$P(\Delta\rho/\rho$=1%) (bar)	P_{max} (bar) (Hammer Pressure)	$\Delta\rho/\rho$ (%) at P_{max}
SW	120	15	1.4	18	12.5
IW	140	16	2	23	11.7
DW	140	16	2	23	11.7

Table 3: Pressure limits for the SPH simulations.

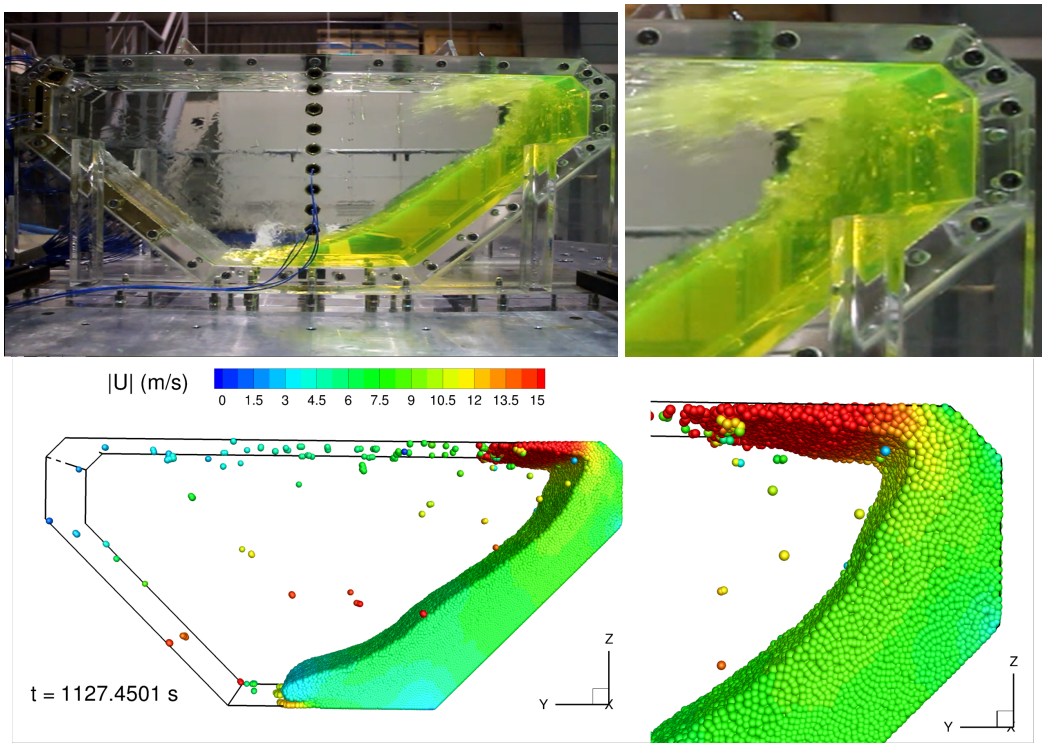

Figure 6: **SW** case. Top left: picture taken from the experiment during an impact event. Top right: enlarged view. The presence of air bubbles inside the bulk of the fluid is evident. Bottom: picture taken from the 3D SPH simulations during an impact event.

equal to $\rho\, c_0\, U_{jet}$ and, therefore, it is strongly dependent on the choice made on the speed of sound. Table 3 reports the different parameters relevant for the present discussion. In the table the maximum flow velocity measured for the three cases in the preliminary 2D simulations have been reported. The $P(\Delta\rho/\rho$=1%) represents the pressure limit in the weakly-compressible regime, it means that pressures below this threshold are expected to be not influenced by the c_0 choice. Conversely P_{max} are related to the water-hammer pressure limit and the density variation related to these values are of order of $\Delta\rho/\rho \simeq 12\%$.

We consider these limits as the maximum reliable pressures in the SPH simulation: when these limits are exceeded the compressibility starts to play a too relevant role and a two-phase model is needed for a better prediction. It is important to note that the adoption of c_0 in the range 120–140 m/s corresponds to the speed of sound of fresh water with 1% of air dispersed as bubbles (for more details see Peregrine (2003)). From figure 6 it is possible to see that different air-bubbles are present in the bulk of the fluid during violent impacts. In this way in our SPH model we estimate 1% of air entrapped in the water. However the model adopted cannot take into account the bubble spatial distribution nor the sizes of the entrapped bubbles. The air bubbles largely influence the rise time and the

time duration of the pressure peaks and, thus, we do not expect that SPH will be able to accurately predict those quantities.

On the other hand it is worth noting that when in our model the pressure hammer limit is reached it means that using an incompressible solver the pressure peak would be unbounded and proportional to $1/\Delta t$. Therefore, with an incompressible solver the pressure peak in those case are completely dependent on the time-space resolution adopted in the simulations. This is not the case for the SPH simulations thanks to the limit linked to c_0 which, in any case, is strictly dependent on the estimation of the volume fraction of air in water during the impact event.

During the liquid impact stages, besides the first positive pressure peak, a series of negative pressure peaks can develop; these are mainly linked to the oscillations of the entrapped gas bubbles. Therefore, the negative pressure phases have an important role in the physics of the liquid impacts. It is worth to note that the negative pressures evaluated in the present simulations are affected both by the tensile instability and by the intrinsic limit of the single phase model. The removal of the tensile instability will require other corrections, like the one proposed in Antuono et al. (2021) or in You et al. (2021). However, the latter can reduce the robustness of the present scheme, making long-time simulations of such violent sloshing flows complex to be handled. This topic deserves further insights with respect to the present analysis which are left for future investigations. The main target and interest from an industrial point of view, indeed, is the measure of the maximum pressure impacts and its statistical analysis for the tank structural design.

4.6. Preliminary 2D simulations with different spatial resolutions

In order to verify that the spatial resolutions, identified in the previous section, are fine enough to get pressure evaluations which are weakly dependent on the particle size, some tests in the 2D framework have been performed. The case **SW** has been selected for this preliminary analysis and different pressure probes are considered in order to check the effect of the Δr parameter. The left plot of figure 7 shows a water impact event obtained with the highest resolution $H/\Delta r = 80$, while on the right plot the pressure probes used in the 2D analysis are depicted.

For the sake of conciseness, the convergence of the SPH solutions is discussed here only for the probes LC6 and T3, these being enough representative also for the other positions.

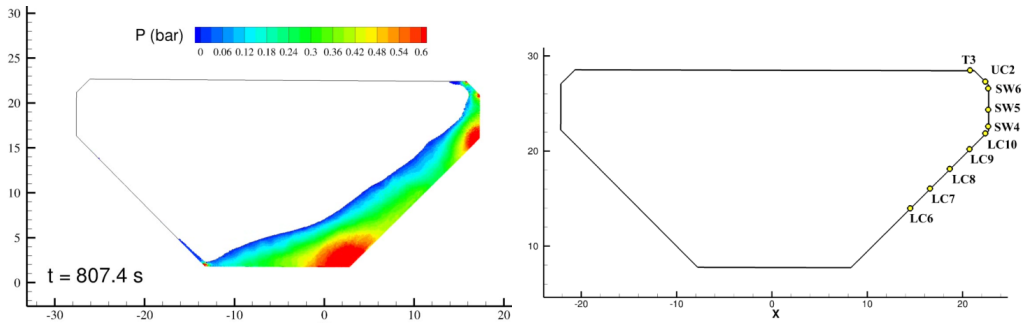

Figure 7: 2D preliminary analysis for the **SW** case. Left: particle configuration during a water impact obtained with the highest spatial resolutions $H/\Delta r = 80$. Right: positions and labels of the pressure probes used in the 2D analysis.

The time histories of the pressure evaluated at the probe LC6 using three different spatial resolutions $H/\Delta r = 20, 40, 80$ are reported in Figure 8. The effect of the particles

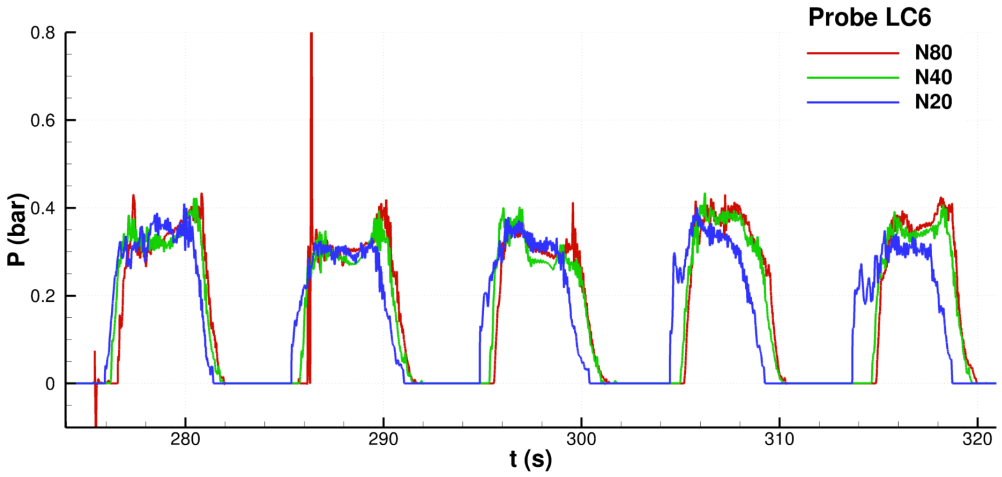

Figure 8: 2D preliminary analysis for the **SW** case. Time histories of the pressure recorded at the probe LC6 using three different spatial resolutions $H/\Delta r = 20, 40, 80$.

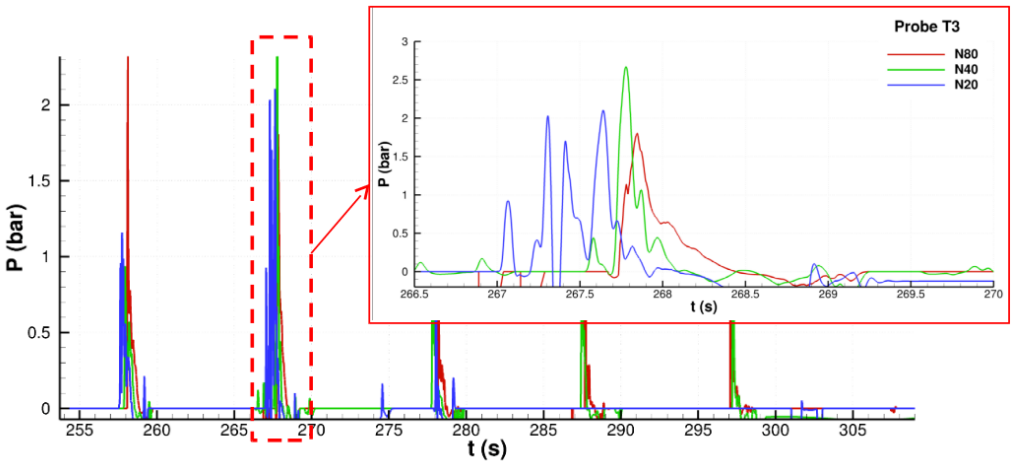

Figure 9: 2D preliminary analysis for the **SW** case. Time histories of the pressure recorded at the probe T3 using three different spatial resolutions $H/\Delta r = 20, 40, 80$.

size on the pressure is limited in this case and, for $H/\Delta r = 40$ and $H/\Delta r = 80$, the pressure recordings are quite close apart from an impact event registered at t=286.5 seconds only with the highest resolution.

For the probe T3 the dependency on Δr is expected to be much higher because the impact on the roof depends on the water jet formed along the lateral side of the tank. By changing the resolution these water jets change in shape causing different loading processes. Further, the thickness of the jets in proximity of the T3 probe is very small and the water impact is resolved only with few particles. Figure 9 shows the pressure time evolution on T3 obtained with the three spatial resolutions. As expected, the effect of the parameter Δr is much higher; this result shows also that with a lower resolution $H/\Delta r = 40$ a higher pressure peak can be recorded with respect the one obtained with $H/\Delta r = 80$. These local differences between the results related to $H/\Delta r = 40$ and $H/\Delta r = 80$ are much smaller when a statistical data process is conducted on the whole pressure peaks recorded within the 11800 seconds.

The conclusion of the 2D analysis shows that the resolution $H/\Delta r = 40$ can be a good compromise, in terms of accuracy and computational costs, for conducting a 3D

simulation for the case **SW** .

4.7. Extraction of the peak sequences from the pressure time histories

In the present section the Peak Over Threshold (POT) procedure to extract the pressure peaks from the SPH time histories is described. In order to identify a water impact in the pressure signals a first threshold equal to $P_{threshold} = 1.25$ bar (in ship scale) has been considered. For the probes positioned at the lower part of the tank, where also the hydrostatic components are relevant, the above threshold is considered after subtraction of the static component.

Figure 10 shows the SPH pressure time history for the case **SW** on a time window of 500 seconds recorded at the probe LC6. Five water impacts on LC6 have been identified. In the following discussion we focus on the fourth impact. Top plot of figure 11 depicts an enlarged view around the water impact registered at time $t \simeq 11,127.8$ seconds. In this case the maximum pressure P_{max} and its halved value are used to determine the rise and decay times, corresponding to 8 and 11 ms respectively. The order of magnitude of these values is not so far from the experimental ones, in model scale the rise and decay times are 1.13 and 1.55 ms.

In bottom plot of figure 11 the rise and decay times for the same pressure peak are evaluated using P_{max} and $P_{threshold}$ being this second approach more often used in practice. With the latter procedure the time duration of the pressure peak becomes much larger. This can be explained considering that the SPH particle interactions act within the kernel support which is greater than the particles size. As a consequence the pressure rise can present a small plateau preceding the pressure peak which, in turn, induces an enlargement of calculated rise time and decay.

Figure 12 shows a second enlarged view around two other pressure peaks recorded at probe LC6. Also for these two cases, evaluating the rise time with $P_{threshold}$ one obtains values close to $\sim 16-17$ ms at ship scale (2.2 - 2.4 ms at model scale). This characteristic times are not so far from the experimental ones, even if, we will show in the next sections that higher rise times are obtained for other impact events. It is interesting to underline that also for the time history shown in figure 12 a pre-load condition is obtained by the SPH model before reaching the maximum pressure peak, this kind of behavior is responsible for most of the rise times which resulted larger than the ones measured in the experiments.

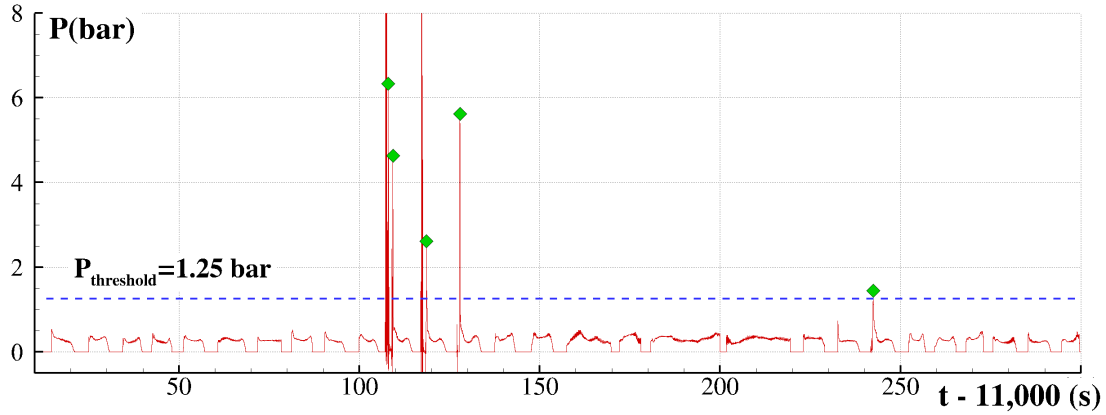

Figure 10: **SW** case. time histories of the SPH pressure recorded at the probe LC6 within the time window 11,000 - 11,500 seconds with a selection of some pressure peaks.

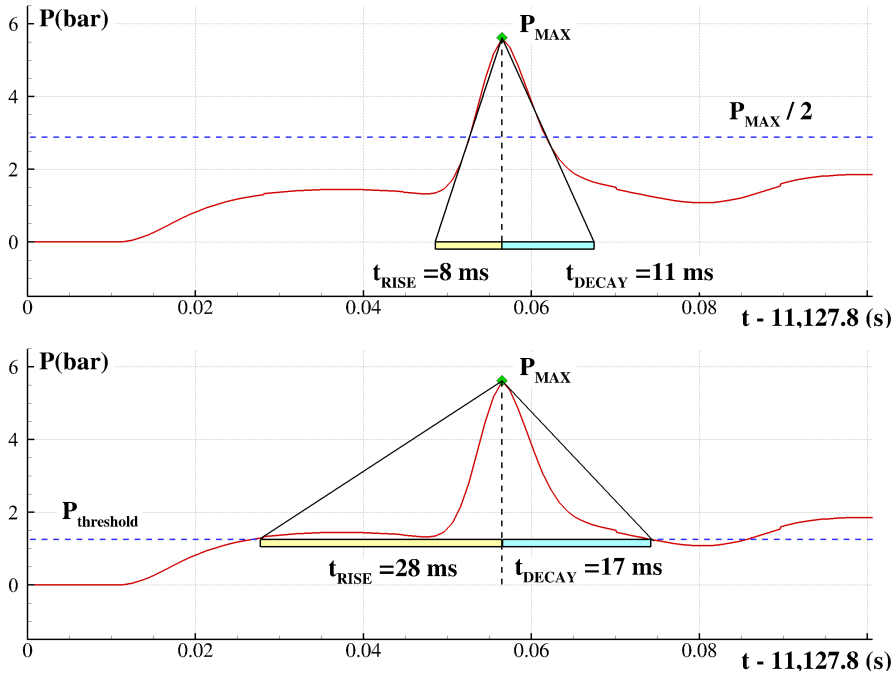

Figure 11: **SW** case, enlarged view around one of the pressure peak selected for the probe LC6. Evaluation of the rise and decay times related to the peak using the halved value of the pressure peak (top) and using the pressure threshold (bottom).

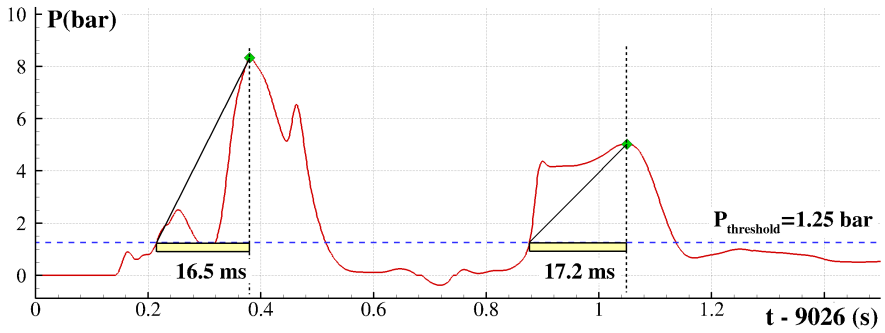

Figure 12: **SW** case, enlarged view around two pressure peaks selected for the probe LC6. Evaluation of the rise and decay times related to the peaks using the pressure peak.

5. Discussion of the results

In this section the analysis of the pressure time histories calculated with the SPH 3D simulations is performed for the three different cases: **SW** , **IW** and **DW** . The most critical probes are here considered and discussed in detail while, in the next section, all the time histories on the 40 probes are considered on the base of the statistical analysis. Specifically, for each filling height we selected the four most critical probes, analyzing in detail the pressure time history. The selected probes are:

- LC6, SW7, UC3, T2 probes for the **SW** case
- LC15, SW7, UC3, T4 probes for the **IW** case
- UC3, T2, T3, T4 probes for the **DW** case:

Each filling condition is treated in separate subsections.

*5.1. **SW** case*

The **SW** case is characterized by very large water displacements and deformations. Figure 13 depicts the particle configuration for two time instants related to an impact event: when the pressure at the wall reaches its maximum (left plot) and when a fast water jet moving along the tank roof is formed and fragmented (right plot). Because of the violent impact the water jet hitting the tank roof is fragmented in several drops.

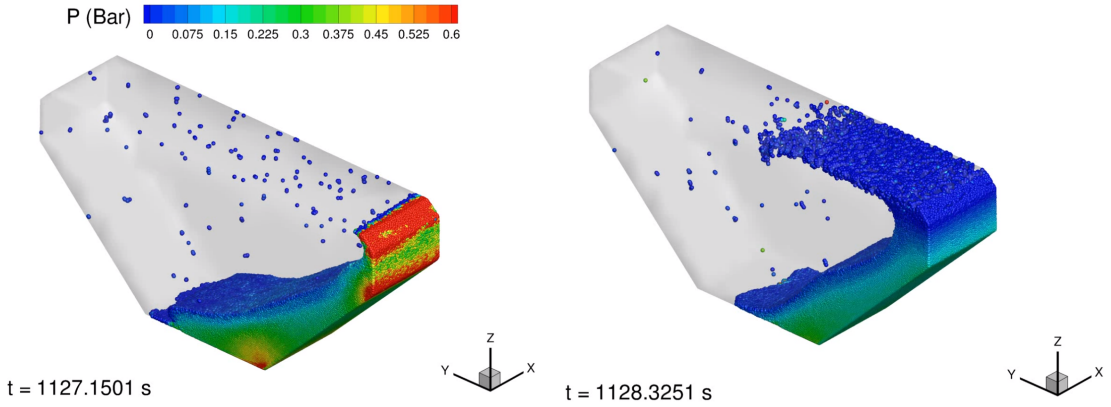

Figure 13: Case **SW** : particles configuration during an impact event for two time instants. Left: the pressure at the wall reaches its maximum. Right: fast water jet at the roof generated after the impact. Colors are representative of the pressure field.

This kind of motion is visible also in the experiments (see figure 6). This flow condition can be critical for mesh-based solver since the size of those drops can be of the order of the mesh-size and, therefore, some of them can be numerically canceled, resulting in a progressive reduction of the water mass. Those kinds of error can be quite critical in long-time simulations where several water impacts take place. Conversely, thanks to the intrinsic mass conservation of the SPH scheme the small drops consisting in single SPH particles are always tracked until they get back into the bulk of the fluid.

Figure 14 shows the pressure peak sequence in the time range 5000–11800 seconds for the probes: T2, UC3, SW7 and LC6. The probe LC6 is positioned in the bottom part of the side wall at about 6.22 m from the tank bottom. LC6 is very close to the still water level for the **SW** condition and, hence, it is cyclically in wet and dry conditions.

The water impact events registered at the probe LC6 are 132 and for six events a pressure level around 20 bar is reached. As we already commented in section 4.5 this pressure regime is related to the hammer pressure level. For the probe SW7 the number of the impact events registered is much higher, 573, the most critical events are again close to the 20 bar level. The same pressure levels are reached also on the probe UC3 and T2 for which the impact events registered are 305 and 257 respectively.

Figure 15 shows for the four considered probes the plot of the pressure peaks versus their rise time. The quantities in these plots have been reported in model scale to simplify the comparison with the experimental data.

Left plot of figure 16 shows the time history of the maximum experimental pressure peak recorded by probe UC3. The maximum pressure peak is about 55 kPa whereas the maximum SPH pressure recorded is about 42 kPa. The magnitude of the recorded SPH pressure is comparable with the experimental data but this is not the case for the rise time. The SPH predicts a rise time of about 2 ms while in the experiments it is about 0.3 ms. The main reason of this discrepancies is probably linked to:

- the low sampling rate of the SPH simulation, 9 kHz, with respect to the 20kHz adopted in the experiments. The SPH sampling rate is linked to the spatial resolution adopted in the simulations, therefore the use of higher resolution can improve the evaluation of the rise time.

- the use of a single-phase model; in reality the time duration of the pressure peaks

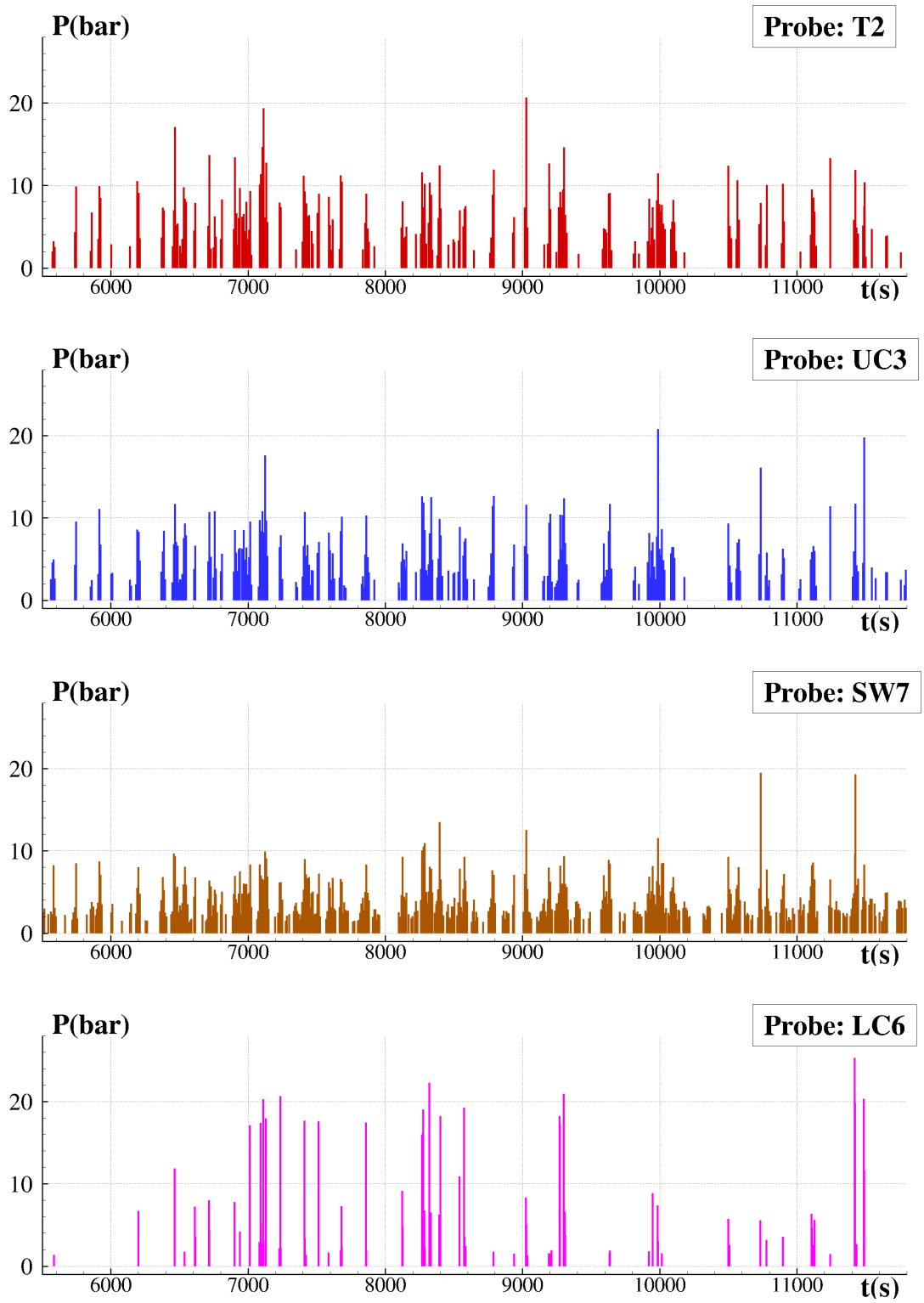

Figure 14: Case **SW** : SPH pressure peak sequences for some of the most critical probes.

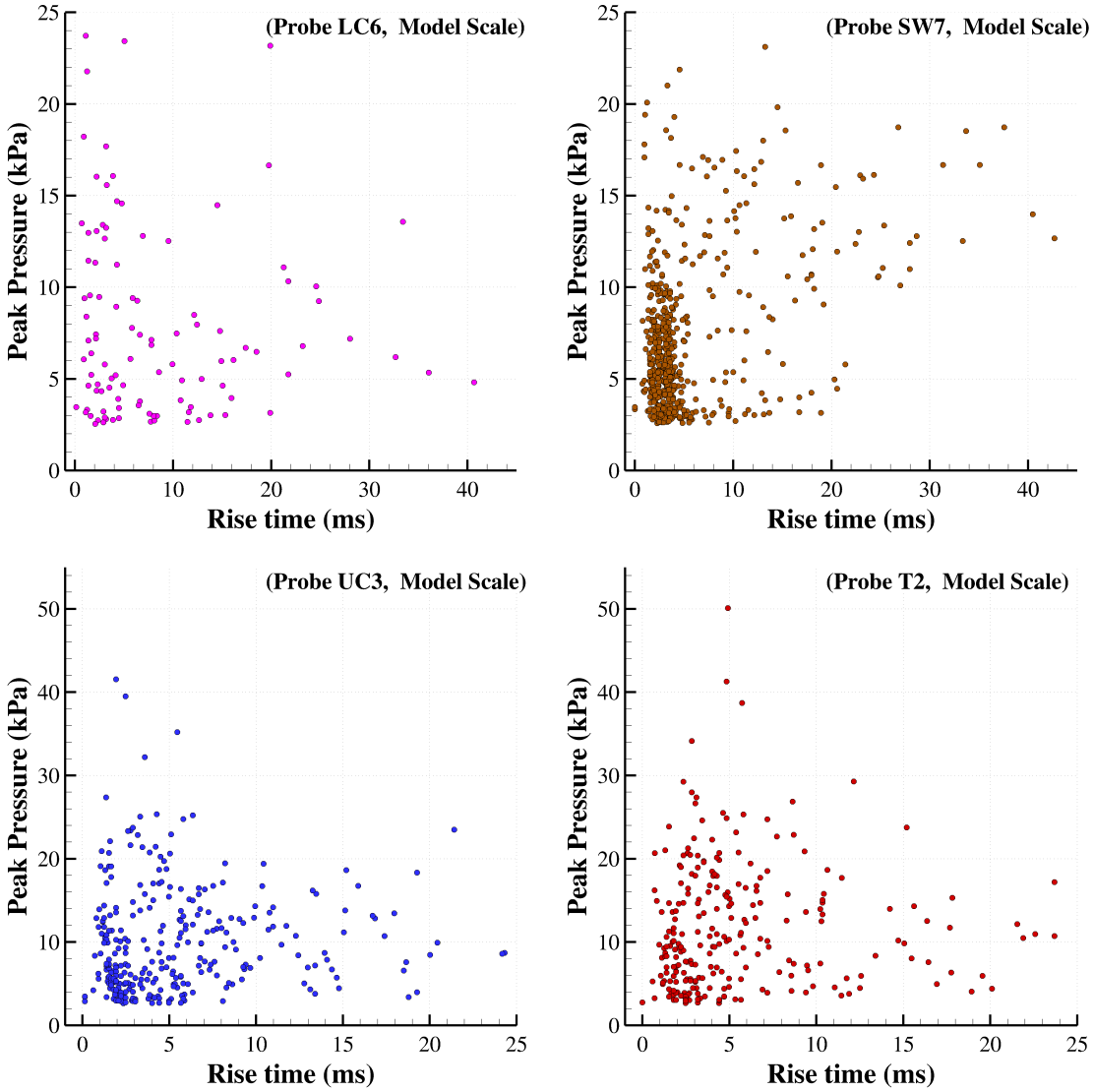

Figure 15: Case **SW** : SPH pressure peak vs rise time for some of the most critical probes (quantities are reported in model scale).

are, indeed, mainly linked to the air pockets entrapped in the water which induce shorter time rises.

- as commented in the previous section the SPH solution tends to predict a pre-loading before the actual pressure peak; this aspect contribute to the increase of the computed time rise.

More research is needed on this topic also to determine the effect of the weakly-compressible model adopted on this specific aspect and to develop possible solutions in order to improve the solvers prediction. Right plot of figure 16 shows the comparisons between SPH solution and experiments data where a scatter diagram for peak pressure and rise time for the **SW** case for the probes LC6 and UC3 is plotted. From this diagram again we get a further confirmation that the SPH is able to predict the peak pressure in a good agreement with the experiments while significant discrepancies occur for the rise times. The SPH evaluate rise times in average about 7 time larger than the experimental recorded ones.

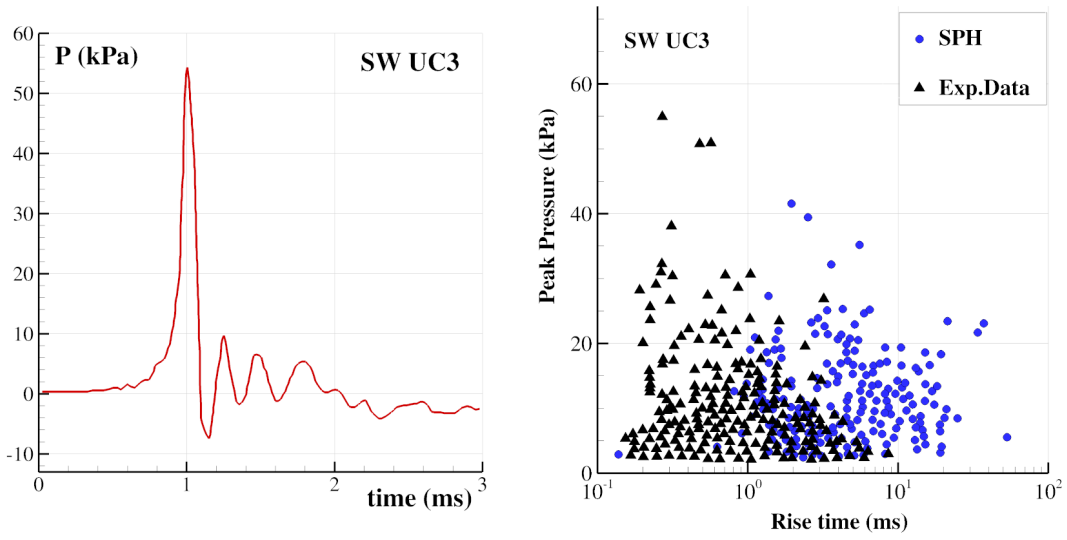

Figure 16: Case **SW** . Left: Time history of the extreme experimental pressure peak record by the probe UC3. Right: Comparison SPH vs experimental data of scatter diagram for peak pressure and rise time at 30%H filling for the probes UC3. The data are reported for the model scale.

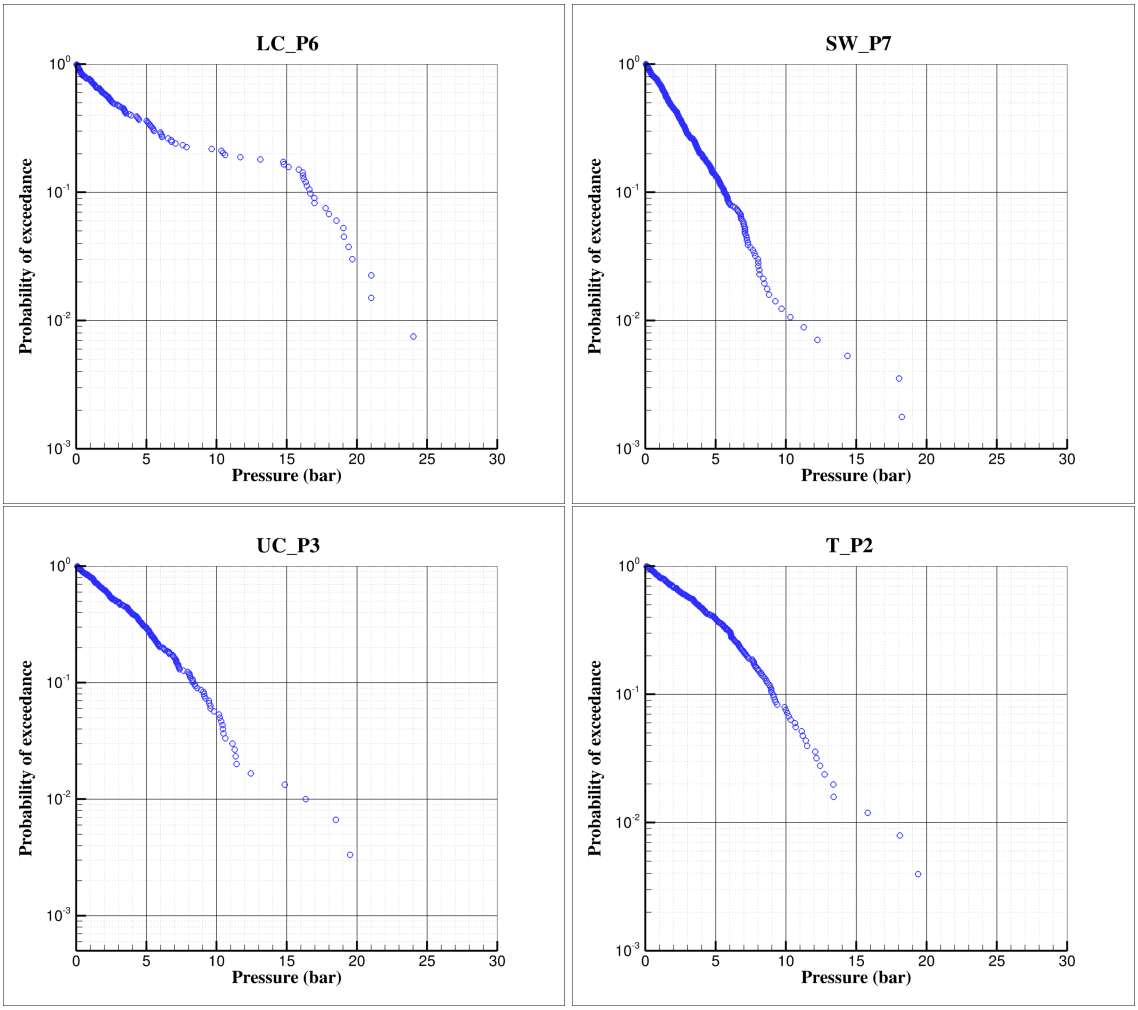

Figure 17: Case **SW** . SPH probability of exceedance evaluated for some of the most critical probes (pressures are reported in ship scale).

Finally, for each considered probe all the pressure peaks identified by the POT procedure have been ordered to evaluate the cumulative probability associated to a specific water impacts with a given pressure intensity. For each event the probability of exceedance E_i has been defined as follows:

$$E_i = 1 - \varepsilon_i; \qquad \varepsilon_i = \sum_{j=1}^{i} \frac{n_j}{n+1}, \tag{8}$$

where n is the total number of registered peaks in POT procedure for the specific probe, ε_i is the cumulative probability associated to the i-th event of the ordered impact sequence. The result of this elaboration is reported in figure 17 where the pressure peaks are plotted against their probability of exceedance (in log scale) for the four probes analyzed in the **SW** case (LC6, SW7, UC3 and T2). The probe LC6 presents a probability distribution with a peculiar behavior which is mainly linked to specific configurations of the flow when this probe is concerned.

5.2. *IW case*

The SPH prediction for the case with intermediate filling height, H=12.44 m, is discussed in this section. This case can be the most critical in some conditions, indeed the filling height still allows large motions of the sloshing flow and, at the same time, it is high enough for the liquid to reach and violently impact the tank roof. Figure 18 shows the particle configuration during an impact event; in this case the pressure $P_{threshold}$ defined in section 4.7 can be easily overpassed. The number of impacts on the probes T2 and T4 is indeed about 350 while for the **SW** case is about 250.

Figure 19 shows the pressure peak sequences in the time range 5000-11800 seconds measured at the probes T2, UC3, SW7 and LC15. For the intermediate filling height most of the LC probes are immersed. With respect to the **SW** case, the most critical probes of LC group are the LC5, LC10 and LC15 which are 1.6 meter above the still water level and are cyclically in wet and dry conditions. Below only the LC15 is considered. Probes SW1 and SW7 are the ones where the largest number of impacts is recorded: about 500 events. From figure 19 it is possible to see that on those four probes 8 critical events with pressure intensity above 50 bar are registered. This pressure level is above the

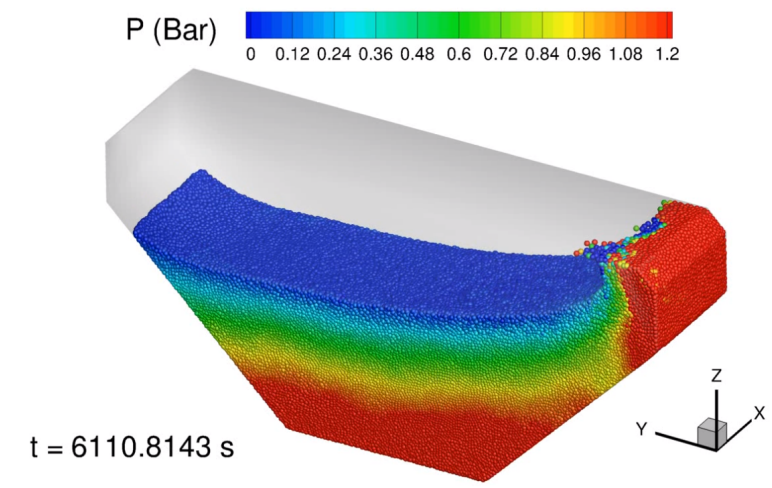

Figure 18: Case **IW** : particles configuration during an impact event. Colors are representative of the pressure field.

limit of the hammer pressure defined in section 4.5 or, in other words, those eight water impacts are largely affected by the selected speed of sound c_0 (see sections 4.1 and 4.5 for details). With a c_0 equal to 140 m/s, the pressure level of 50 bar implies a compressibility of the water-air mixture of $\Delta\rho/\rho$ of about 25%. This means that for these critical events the adopted model is being strained beyond its limits of applicability and these extreme events with $P > 50$ bar ($P > 100$ kPa in model scale) cannot be considered as realistic. Therefore, $P = 50$ bar is considered as the maximum pressure limit acceptable. Each time the code gives pressure peaks higher than this threshold the maximum value will be set to 50 bar (100 kPa in model scale).

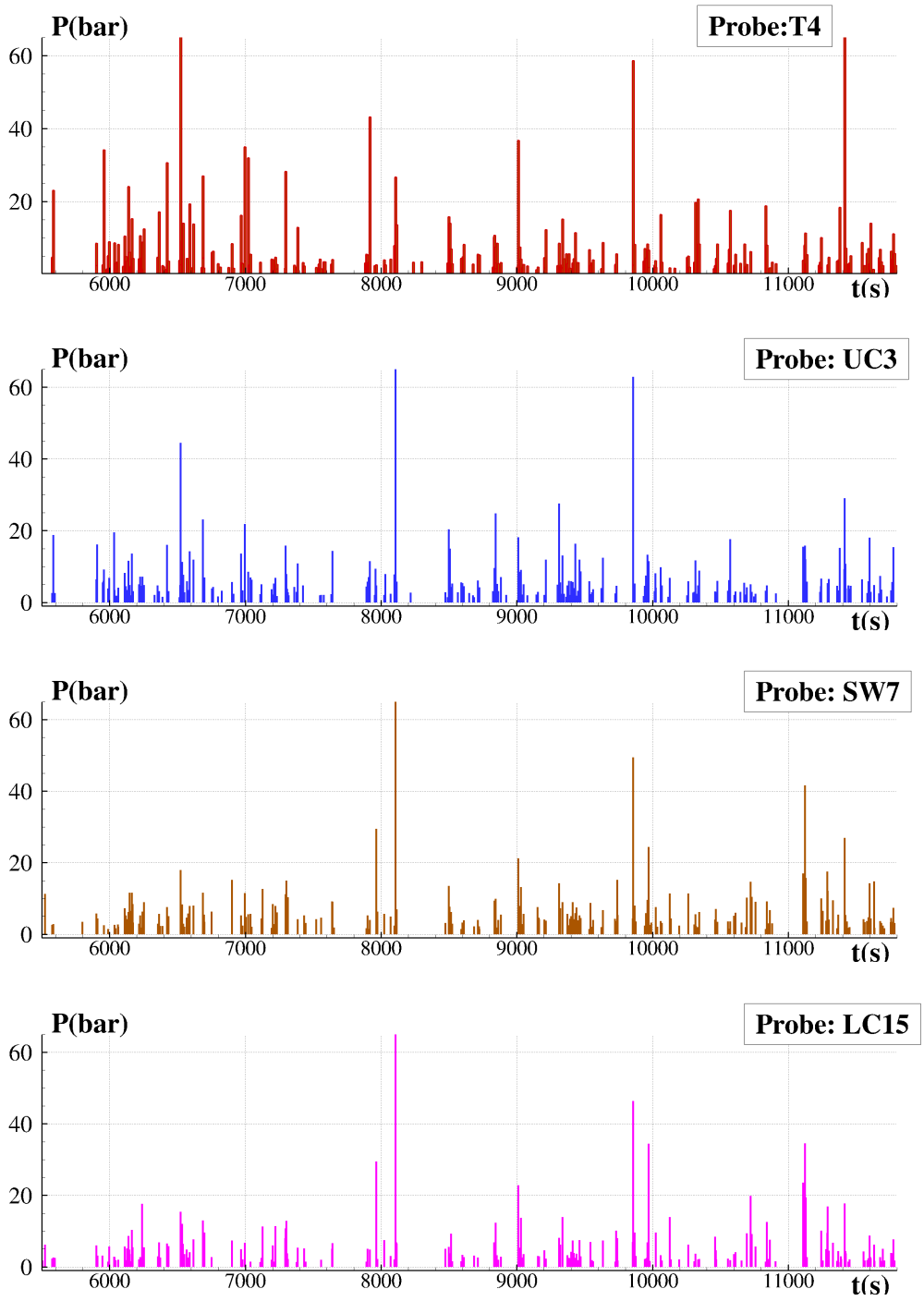

Figure 19: Case **IW** : SPH pressure peak sequences for some of the most critical probes.

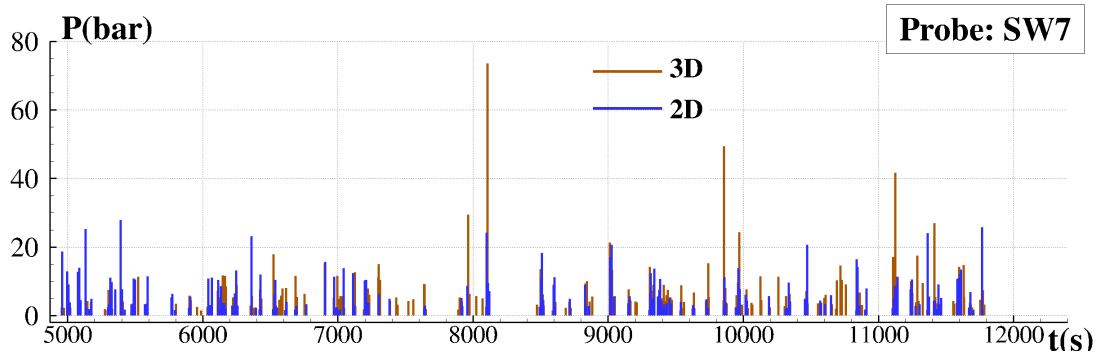

Figure 20: Case **IW** : Comparison between 2D and 3D conditions of the SPH pressure peak sequences for the probe SW7.

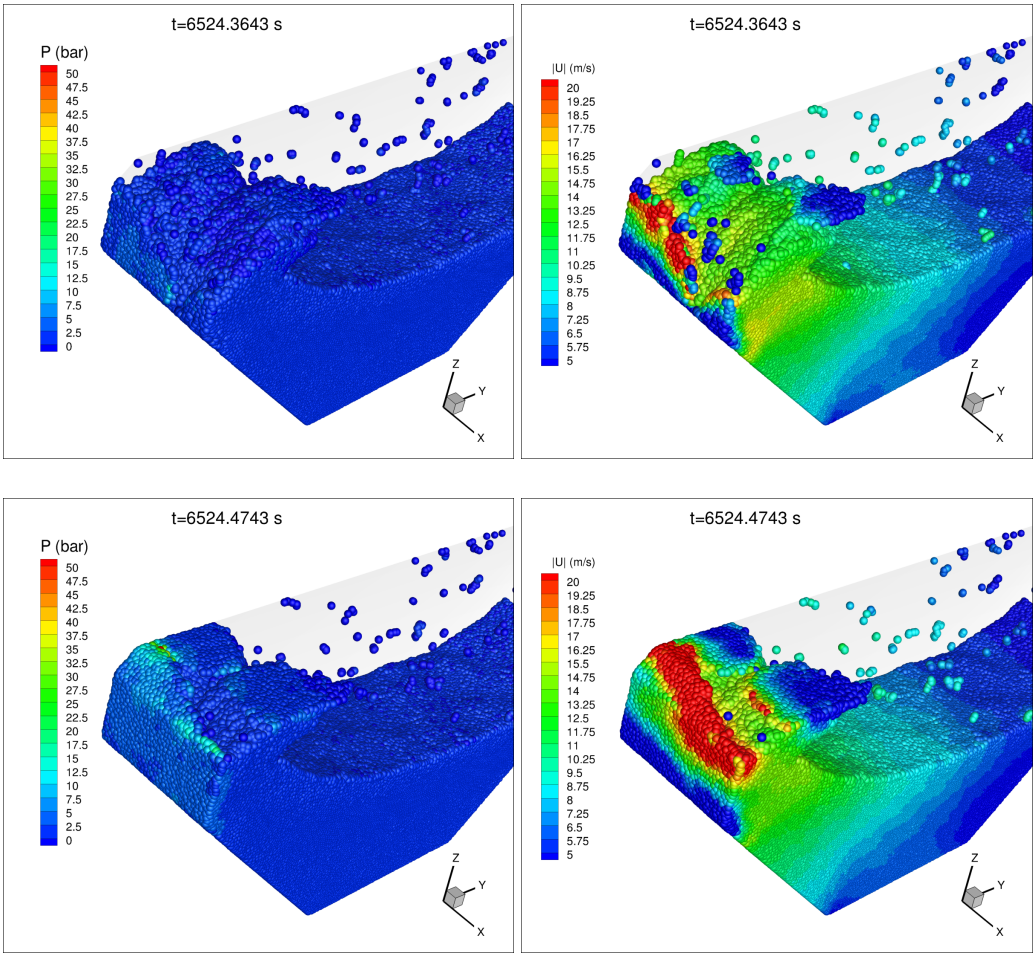

Figure 21: Case **IW** . First two snapshots of a sequence of cavity collapse. Left column: pressure fields. Right column: velocity modulus.

It is worth noting that the extreme events $P > 50$ bar were not predicted by the 2D preliminary analysis we performed before starting the 3D simulations. This is also confirmed by the plot of figure 20 were the peak sequence for the probe SW7 is reported from the 2D and the 3D simulations. From the 2D simulations all the peaks are below 30 bar; this means that event $P > 50$ bar are related to some peculiar 3D flow features.

The flow process which gives rise to those unrealistic pressure peaks is shown figure 21 and 22. When the flow comes from a stage of violent motion the jet climbing the

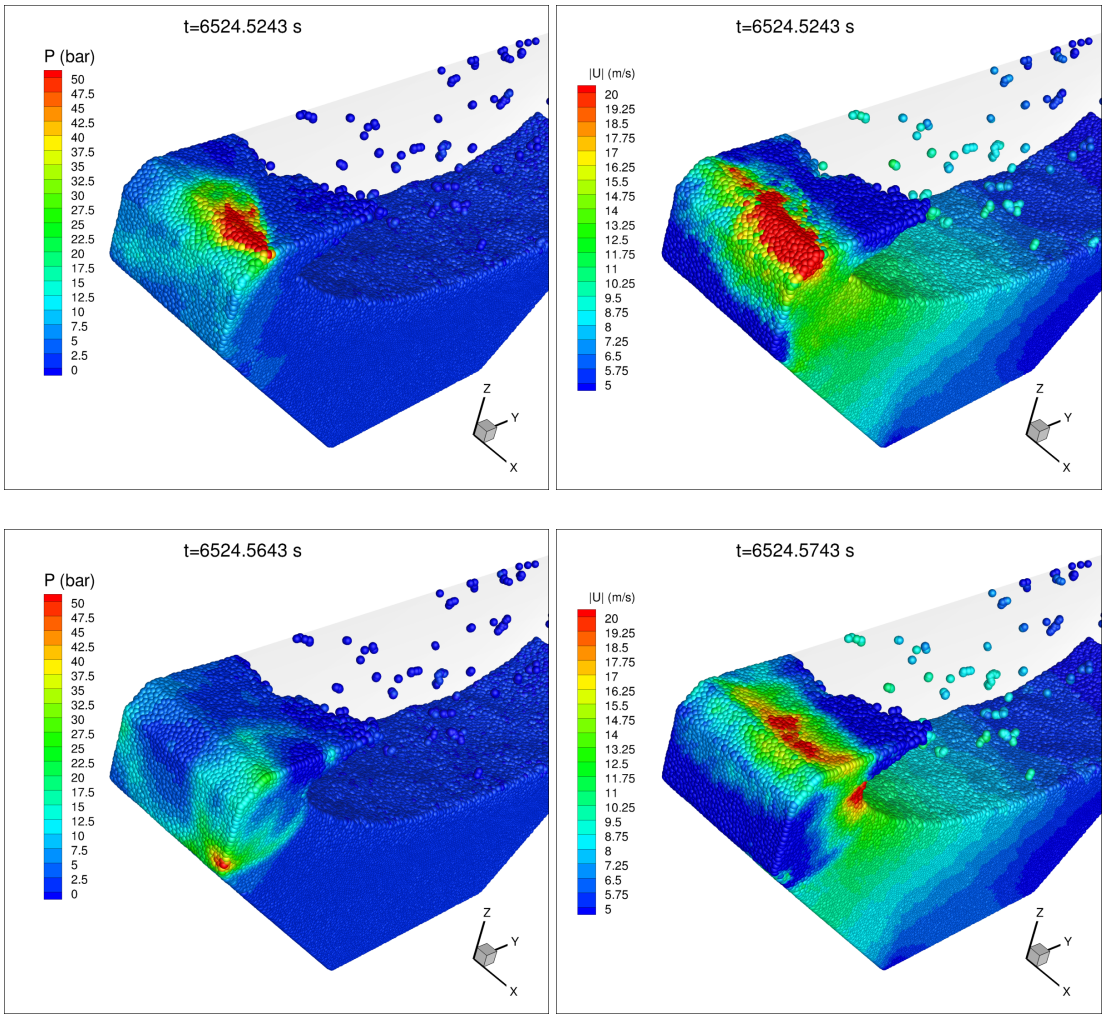

Figure 22: Case **IW** . Last two snapshots of a sequence of cavity collapse. Left column: pressure fields. Right column: velocity modulus.

oblique wall can be characterized by an irregular shape, as shown in the top row of figure 21. In this case, the jet is divided in several parts, some of them impact on the roof while the bulk of the flow follows at high speed the shape of the lateral wall (second row of figure 21). At this stage a void cavity is formed close to the roof vertex which quickly shrinks due to the approaching jets. In the reality this cavity would be filled with air and would induce an oscillating pressure on the probes according to the characteristic air bubble vibration period. Conversely, in the present calculation the void pocket collapses giving rise to a violent fluid-fluid impact which reaches the water hammer pressure limit (first row of figure 22). This pressure easily overshoots 50 bar depending on the relative velocity of the impacting fronts. At the end of this process, a shock wave is released which unloads the compressed region and expands with spherical symmetry focusing on the edges of the tank (last row of figure 22).

The pressure peaks induced by this flow dynamics are shown in figure 23. In the top plot the impulsive character of the phenomenon is highlighted by the pressure signals recorded on the probes positioned close to the cavity: probes T3, T4, UC2, and UC3. The registered pressure peaks are between 40 and 60 bar and the total peak duration is lower than 50 ms ($\simeq$ 7ms at model scale). In bottom plot of figure 23 the pressure peaks

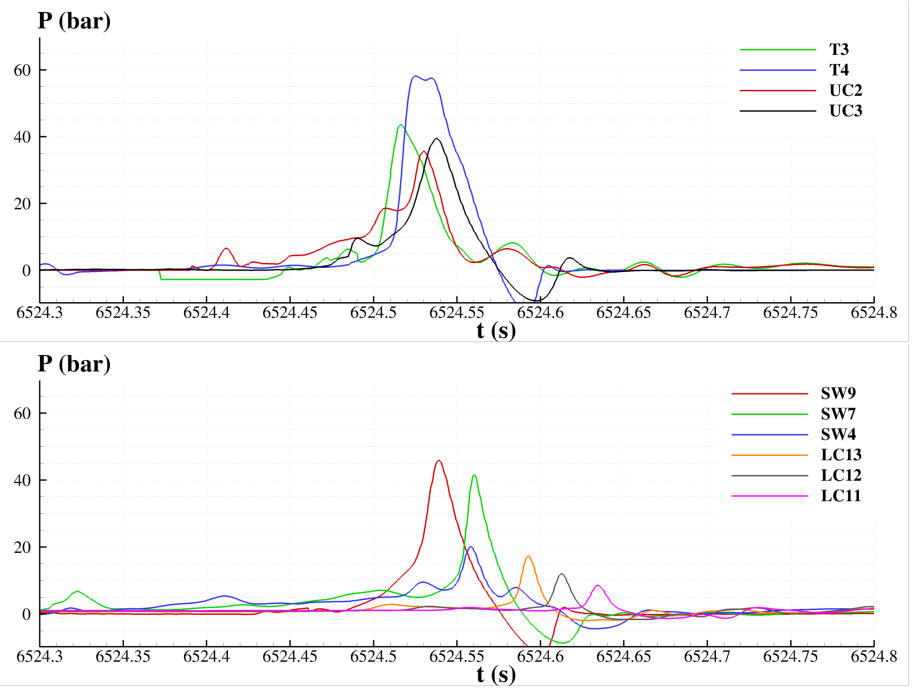

Figure 23: Case **IW** . Pressure signals for the sequence of cavity collapse (see figure 22). Left: probes directly involved in the shock region. Right: probes encountered by the shock wave.

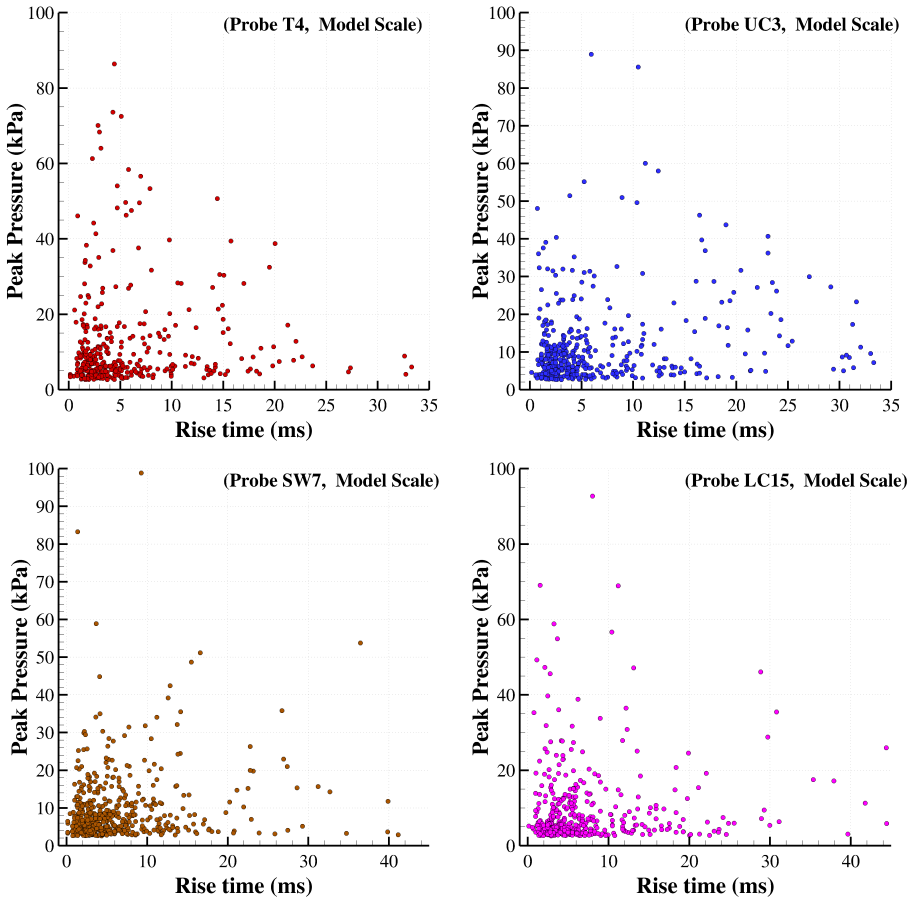

Figure 24: Case **IW** : SPH pressure peak vs rise time for some of the most critical probes (quantities are reported in model scale).

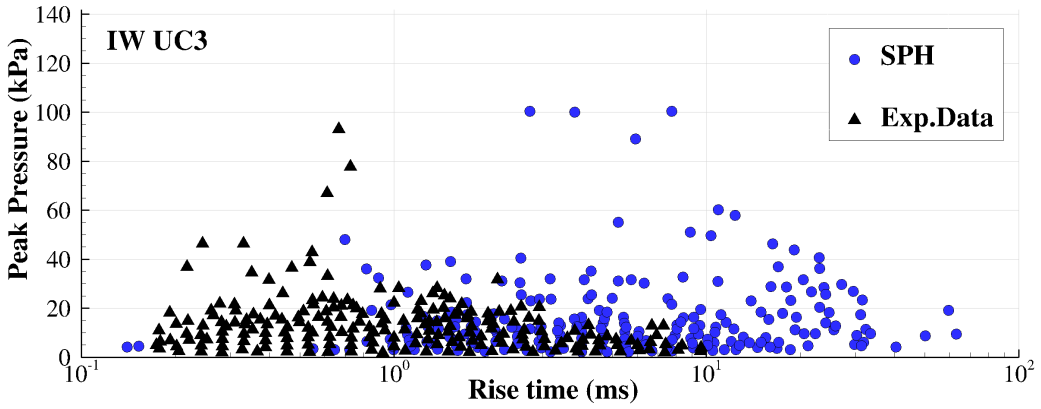

Figure 25: Case **IW** . Comparison SPH vs experiments of scatter diagram for peak pressure and rise time at 60%H filling for the probe UC3. The data are reported for the model scale.

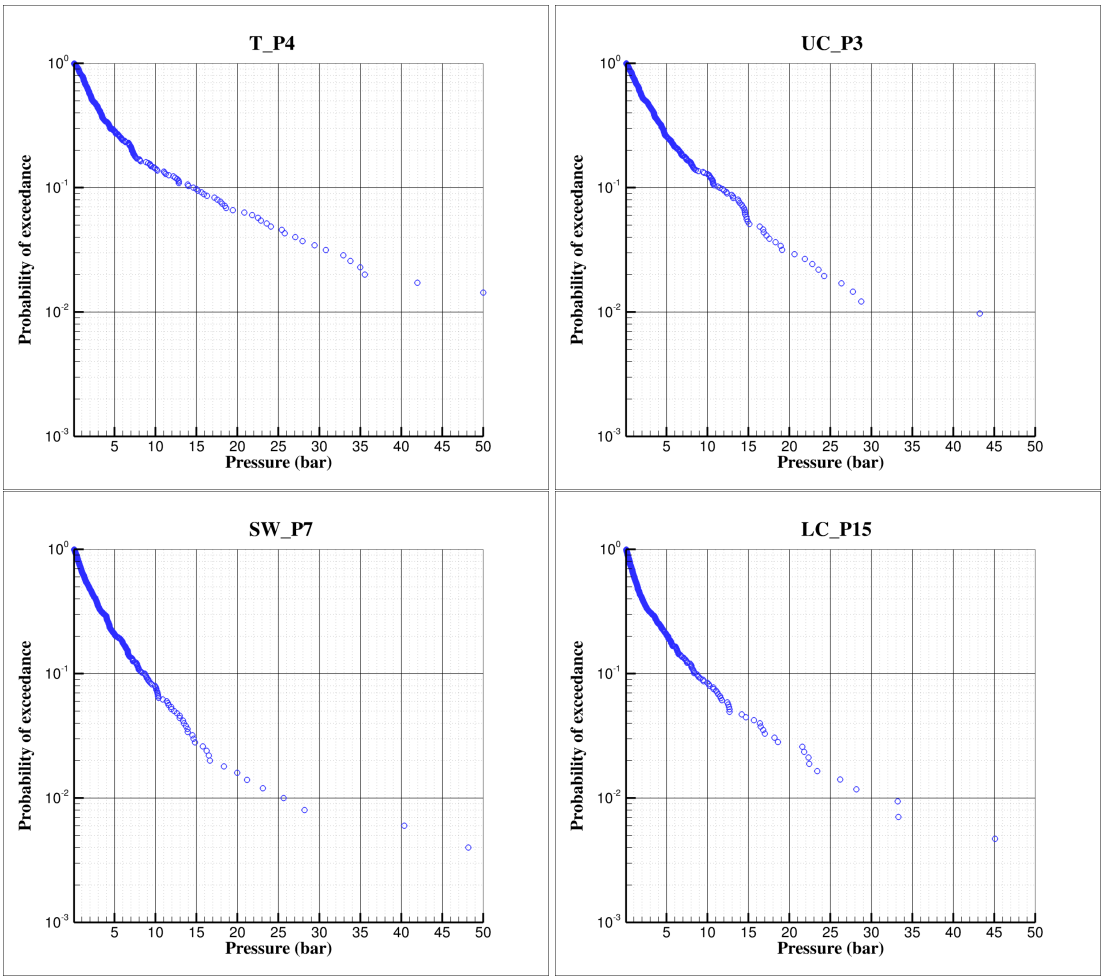

Figure 26: Case **IW** : SPH probability of exceedance evaluated for some of the most critical probes (pressures are reported in ship scale).

corresponding to the shock wave traveling down the tank edge, are shown in the signals recorded at the probes of the groups SW and LC. These probes record a pressure peak in a later time depending on their distance from the region where the shock has originated. The probe SW4, which is approximately at the same distance of probe SW7, records a lower pressure peak being located further away from the edge.

The above described process of cavity collapse is likely to happen more often in

the **IW** case because of the intermediate filling ratio which characterizes this test case. Though interesting, this loading process is strictly related to the limits of the adopted physical model (single-phase approximation) and, therefore, the resulting pressure peak shall be considered as not indicative of the actual pressure attained in reality. The latter, benefiting from the air cushioning effect, is expected to be much less intense (see *e.g.* Marrone et al. (2017)).

Figure 24 shows for the four considered probes the plots of the pressure peaks versus their rise time at model scale. Also in this case the rise time observed spreads up to 40 ms even if most of the events are confined in 10 ms.

Figure 25 depicts the comparisons between SPH and experiments within a scatter diagram where peak pressure and rise time for the **IW** case are plotted for probe UC3. From this diagram the same conclusions of the **SW** case can be drawn: the SPH is able to well predict the pressure peak ranges while the rise times are generally overestimated.

Finally, Figure 26 reports the probability distribution for the probes T4, UC3, SW7 and LC15. With respect to the case **SW** , the behavior of these plots appear more regular due to the higher number of samples. Compared to the **SW** case, this filling condition is much more critical. For all the four probes considered the pressure corresponding to $E = 0.01$ is always larger than 25 bar whereas in the **SW** case it is lower than 20 bar for all probes but one. In particular the curve corresponding to the probe T4 (top-left plot of figure 26) exhibits extremal values which reaches the limit of 50 bar, as already commented.

*5.3. **DW** case*

Finally, in the present subsection the case **DW** , which is characterized by the highest filling height $H = 18.67$ m, is discussed. Figure 27 shows a particle configuration during a roof impact event. This case is characterized by numerous roof impacts and the most critical pressure probes are T2, T3, T4, most of the other probes being completely immersed. The SW3, SW6, SW9 are just 55 cm above the still water level while the UC probes are at a distance of 88 cm. Because of the above observations, in the following analysis only the probes T2, T3, T4 and UC3 are considered; indeed, for each of these, more than 1100 impact events are recorded. Beside this, we note that critical impact events are also recorded at probes SW1 and SW7, as commented in the next section where the statistical analysis is discussed for all the pressure probes.

Figure 28 shows the sequences of the SPH pressure peaks for the probes T2, T3, T4 and UC3 in the time window 5500-11800 seconds. For the probes of the group T, similarly to what shown in the previous case for other tank positions, some violent events induce pressure levels higher than 25 bar (50 kPa in model scale) which is the pressure hammer estimated by the 2D preliminary analysis using the maximum of the velocity field (see section 4.5). Conversely, the pressure peaks for the probe UC3 are always below such a pressure threshold. This is confirmed also by the results reported in figure 29 where the pressure intensity of the peaks is shown against their rise times. As for the latter, again, the range is between 1 to 90 milliseconds, much larger than the one experimentally measured.

Left plot of figure 30 reports an experimental picture taken during the **DW** case (but in a different reference sea-state condition). The middle and the right plot of the same figure depicts the time histories for two pressure peak measured in the proximity of the T2-T4 probes. It is interesting to note that the peak pressure intensities are around 80 kPa, corresponding to 40 - 45 bar in ship scale, hence, quite close to the most energetic events evaluated by the SPH model.

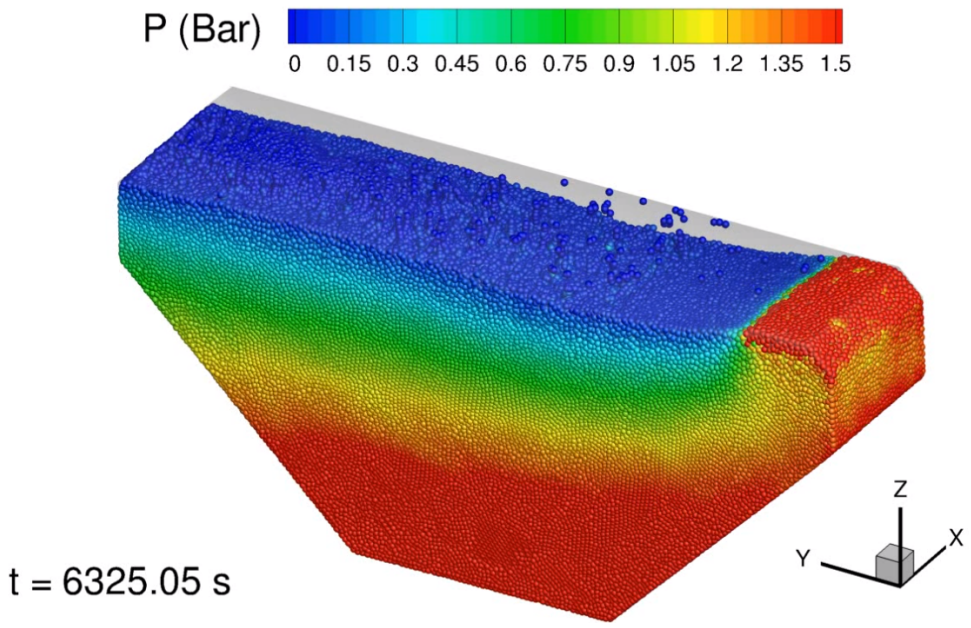

Figure 27: Case **DW** : SPH 3D simulation, particles configuration during an impact event. Colors are representative of the pressure field.

Figure 31 shows the scatter diagrams of peak pressure and rise time for the **DW** case for the probes UC3 and T4. Also for the highest filling height condition the SPH is able to predict the pressure peak ranges in a fair accordance with the experiments while the rise times are again overestimated.

Figure 32 depicts the SPH probability of exceedance for the probes T2, T3, T4 and UC3. The probability distribution is quite regular for pressure intensity below the 15 bar, the number of samples being substantial for this case. A significant difference between the trend of the T probes and the probe UC3 is observed, the latter presenting a less critical slope. Further, it is also evident that probes T2 and T4, which are the ones located at the corner of the tank, have a similar shape and are characterized by higher extremal values when compared to probe T3 (the one placed in the middle of the edge). This behavior was rather expected, as one may easily foresee that water jets mostly focus at the tank corners.

6. Data Processing for the statistical outcomes

In this last section the results given through the statistical analysis on all the pressure probes are discussed for all the three cases simulated, **SW** , **IW** and **DW** . In order to simplify the discussion, the different data are presented through contour plots on the tank surfaces equipped with the pressure sensors. For the sake of completeness, the main statistical quantities are reported for all probes in three tables at end of the section.

In figure 33 the number of water impacts identified in the 3D simulations are reported. For the case **SW** , the largest number of impacts is on the SW1, SW4 and SW7 probes as expected. These probes are positioned just after the first edge on the lateral side and a water jet rising the wall will firstly impact on this region of the wall. Also for **IW** this part of the tank registered the highest number of impacts; however with respect to the previous case, two main differences appear: (i) the number of impacts on the upper part of the tank increases as expected, (ii) the number of impacts is higher in the lateral sides (those at x=0.0 and x=9.86 m, see figure 1) then in the middle probe row (those at x=4.93 m) and this is clearly linked to 3D effects: water jets tend to focus along the vertical edge

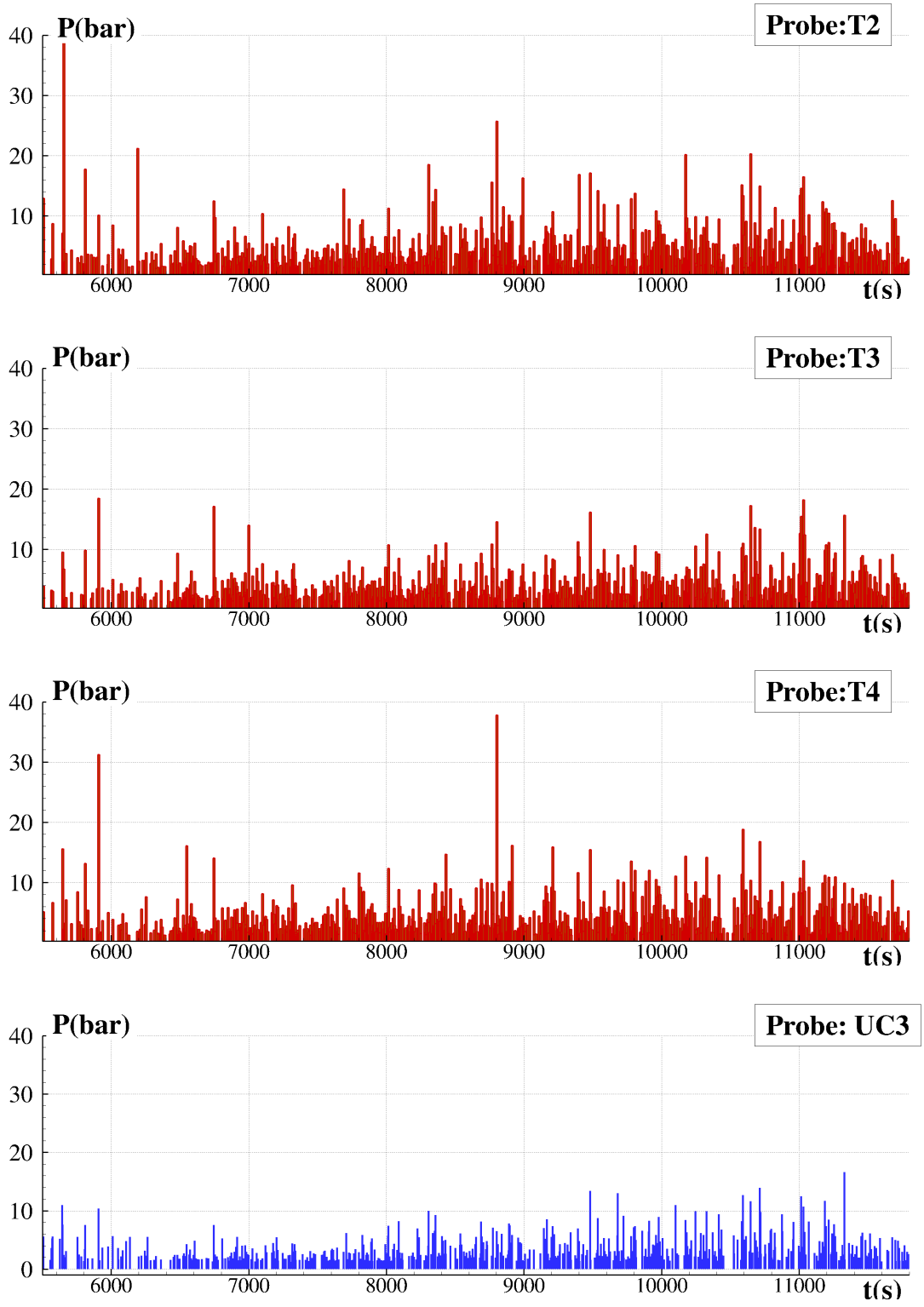

Figure 28: Case **DW** : SPH pressure peak sequences for some of the most critical probes.

of the tank. For both **SW** and **IW** the maximum number of impacts recorded is around 500. This number drastically increases for the **DW** case reaching a value of about 1500. For the **DW** the 3D effects are less evident than the **IW** case.

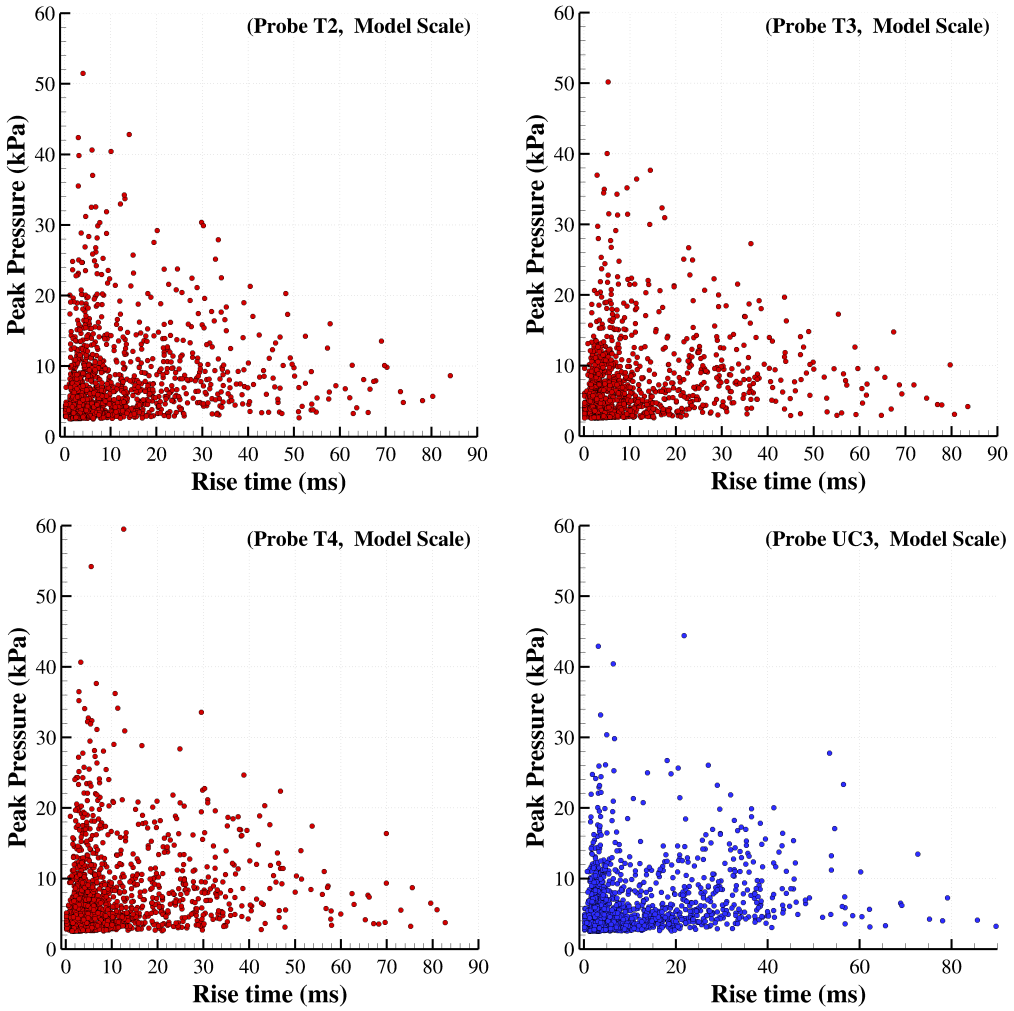

Figure 29: Case **DW** : SPH pressure peak vs rise time for some of the most critical probes (quantities are reported in model scale).

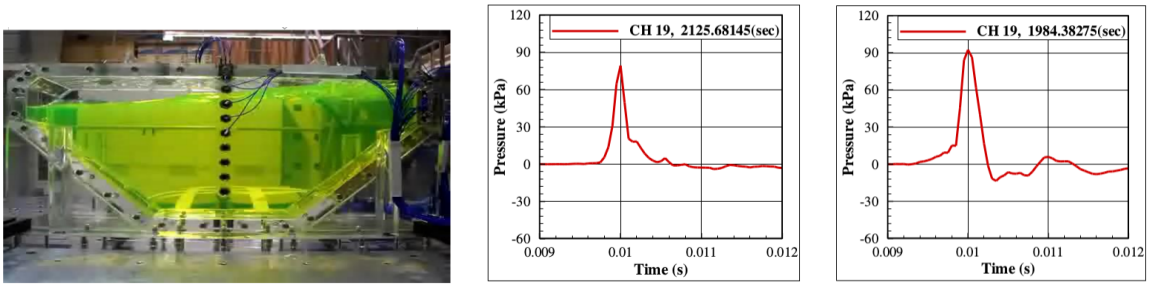

Figure 30: Case **DW** : Left: picture taken during experiments performed with a sea-state given by a Pierson-Moskowitz spectrum with significant wave height 8.3 m and zero crossing period 7.50 sec with an angle condition of 120°. Middle and right: time history of pressure peaks measured at the probe T4 position (quantities are reported in model scale).

Figure 34 reports the average of k-largest pressure peaks evaluated as:

$$p_{avg.k.largest} = \frac{1}{k}\sum_{i=1}^{k} p_i$$

where the p_i are the pressure peaks sorted from the maximum to the minimum value. Values of k equal to [3, 5, 10] are used. When considering only the first three peaks, i.e.

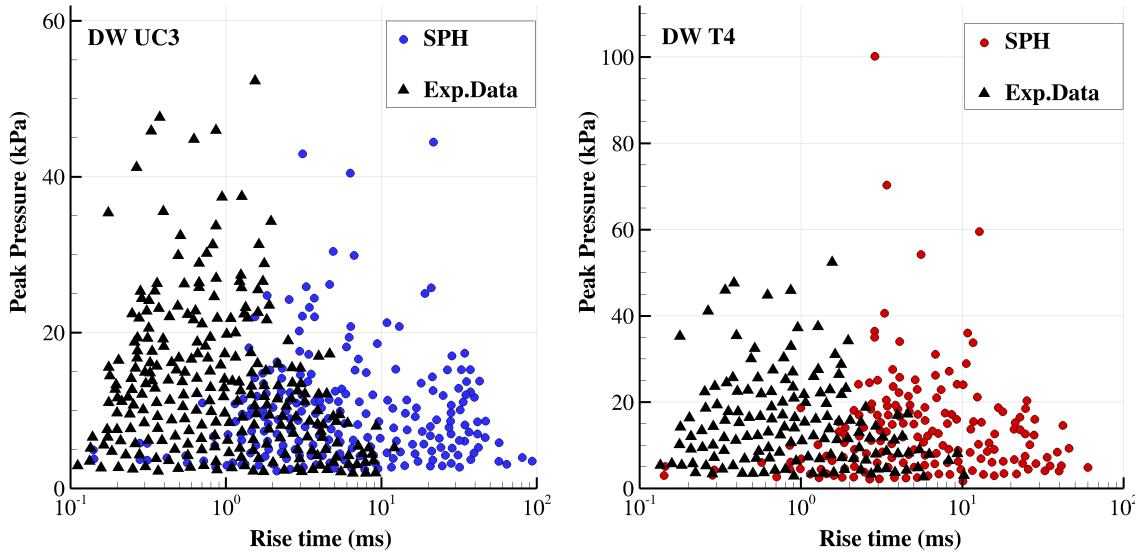

Figure 31: Case **DW** . Comparison of scatter diagram for peak pressure and rise time at 90%H filling for the probes UC3 (left) and T4 (right). The data are reported for the model scale.

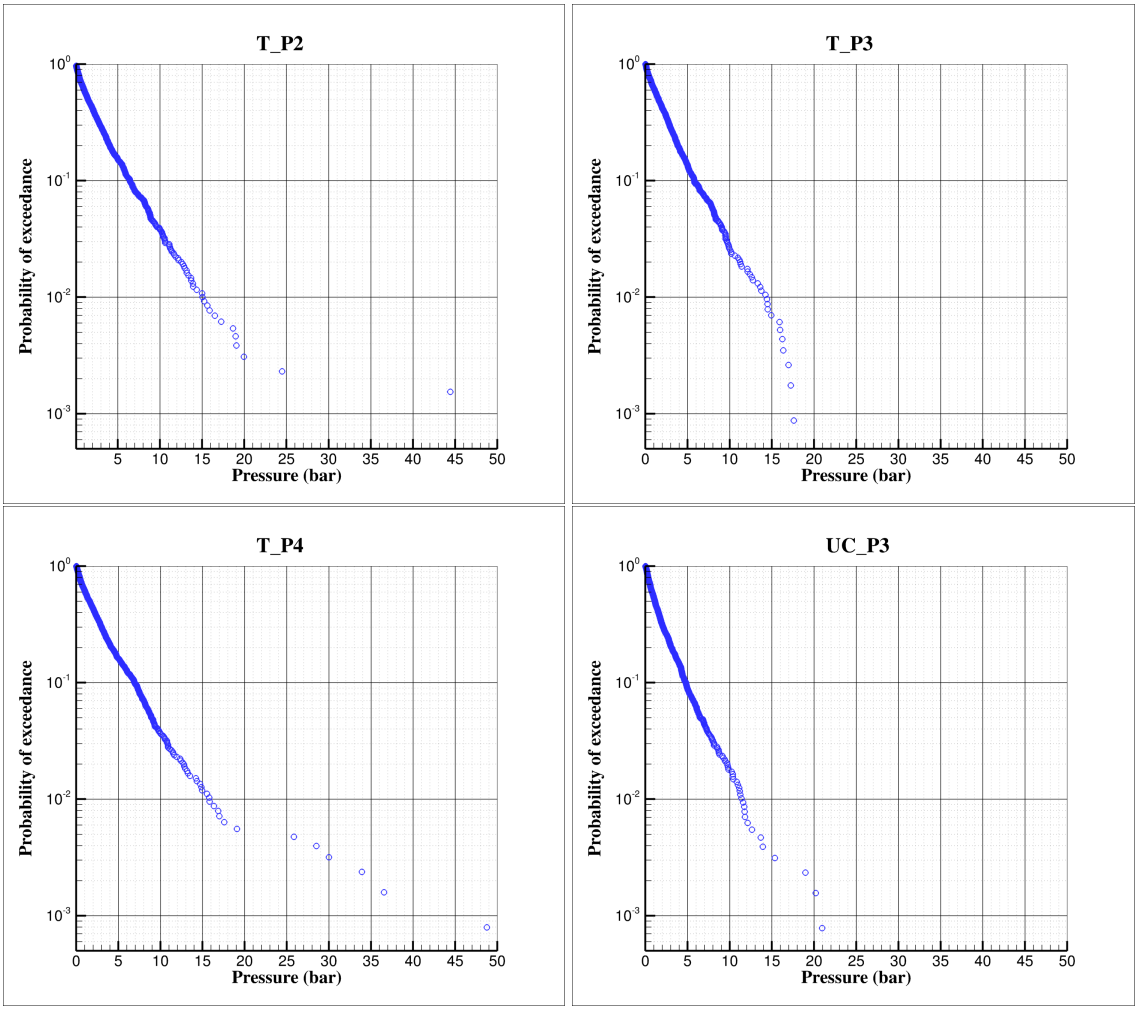

Figure 32: Case **DW** : SPH probability of exceedance evaluated for some of the most critical probes (pressures are reported in ship scale).

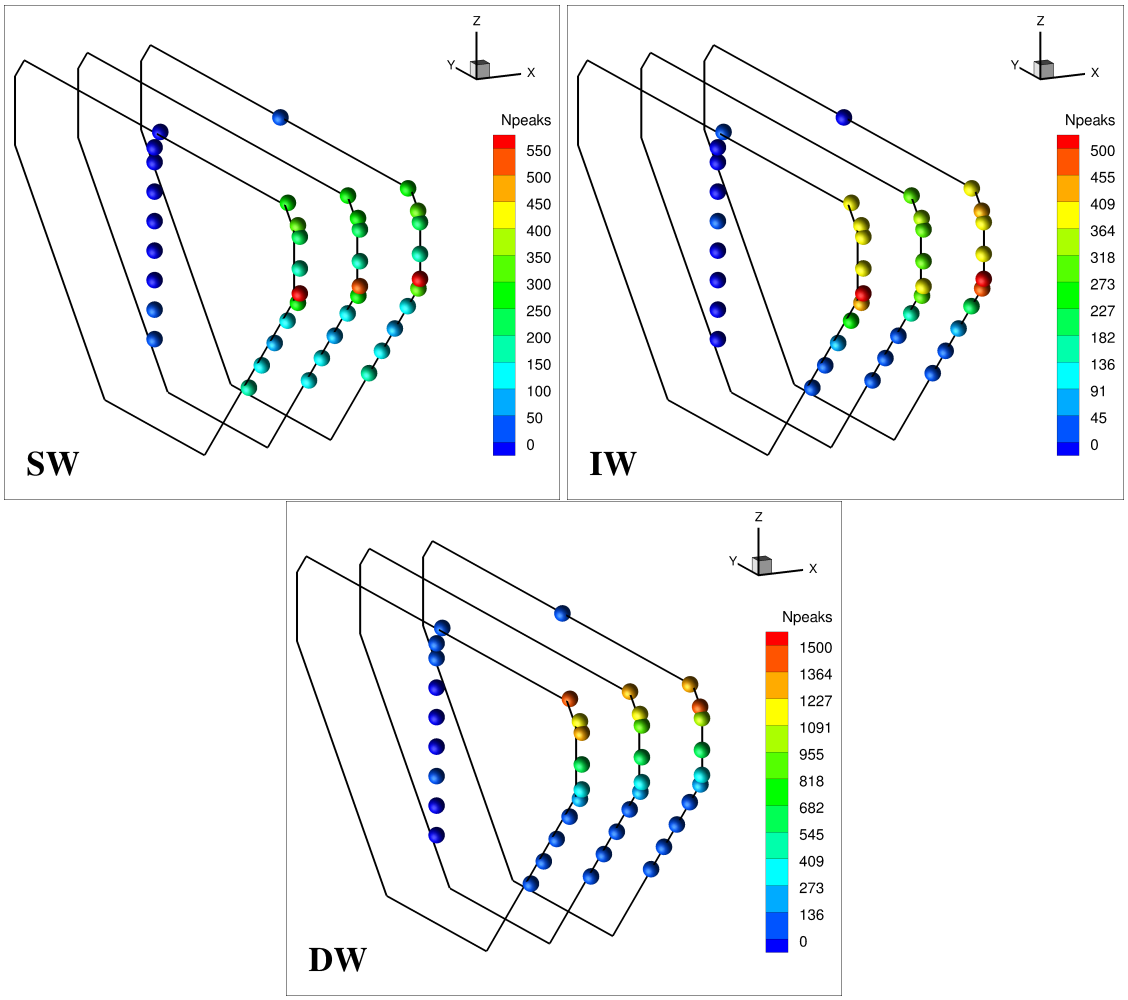

Figure 33: Number of the pressure peaks counted during the simulation for the case **SW** (left), **IW** (middle), **DW** (right).

$k = 3$, for the **SW** the levels of 20 bar is overpassed both on the roof and on the lower part of the lateral sides. When considering $k = 10$ it is more clear that the critical zone of the tank for the **SW** case is the one close to the probes LC1, LC2, LC6, LC11 and LC12. The averages of the k-largest pressure peaks increase a lot when passing from the case **SW** to **IW** .

For the latter the pressure scale is increased up to 50 bar, indeed for k=[3, 5, 10] the average pressure in the upper part of the tank exceeded the 50 bar. As commented in section 5.2 we consider this level unrealistic since the compressibility of the SPH model reaches a too high level. From a practical point of view this means that the use of a single-fluid model is not reliable since air-cushion effects are too relevant and need to be taken into account through a multiphase (gas-liquid) model.

For the **DW** case, the upper level of 25 bar (50 kPa in model scale) is overpassed for both k=5 and 10 only at the probes T2 and T4. The latter results is confirmed also experimentally since in T2 and T4 probes, pressure levels close to 100 kPa in model scale have been registered (see section 5.3).

Additionally to the averages of the k-largest pressure peaks another pressure average is evaluated for the three filling height studied. This second average is on the $1/m$ largest

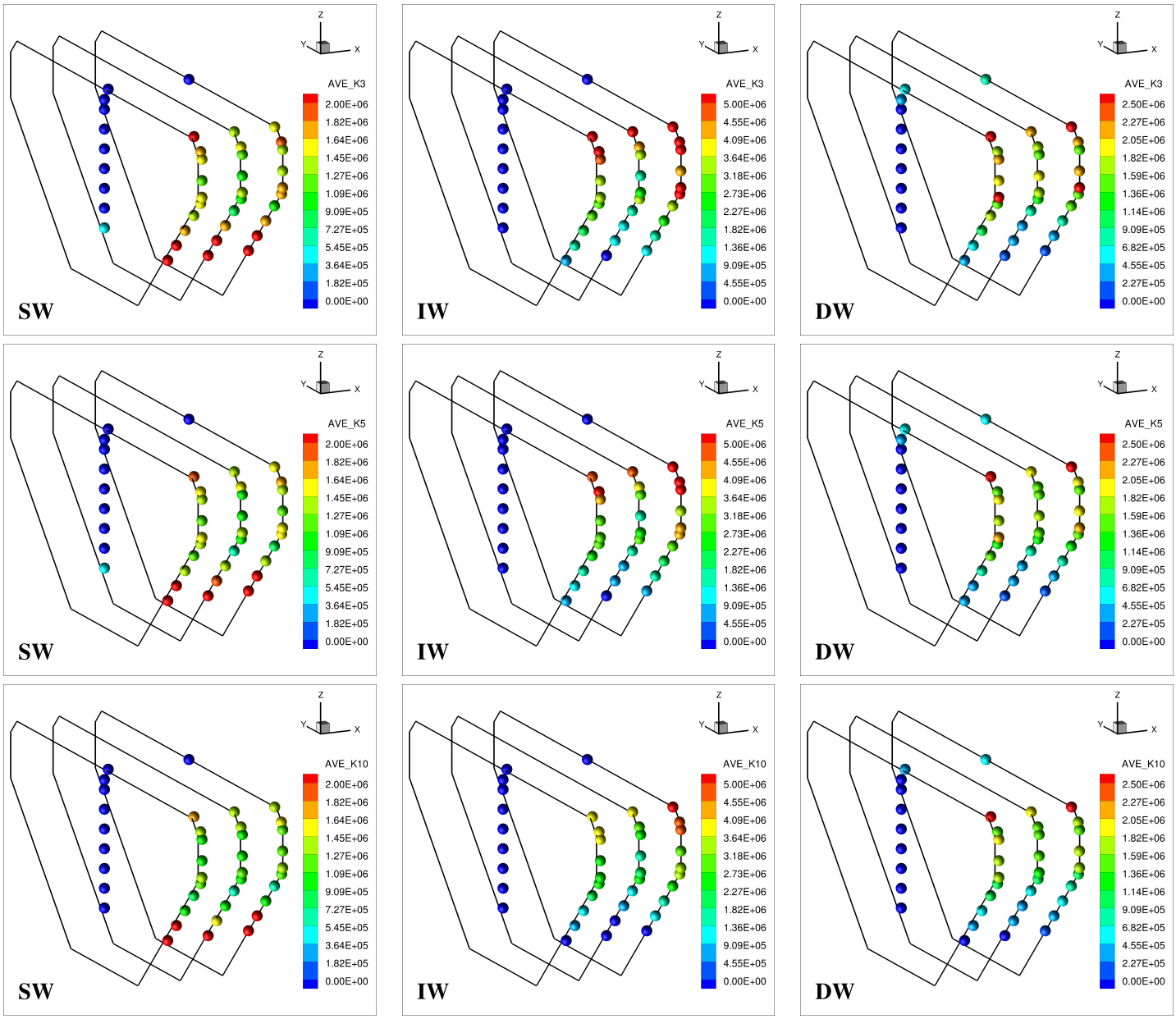

Figure 34: Average of k largest pressure peaks with k=3 (top row), 5 (middle row), 10 (bottom row) for the case **SW** (left column), **IW** (middle column), **DW** (right column).

peaks evaluated as:

$$p_{avg.1/mlargest} = \frac{m}{n} \sum_{i=1}^{n/m} p_i$$

where again the p_i sequence is constituted by the pressure peaks sorted in descending order, while m is a parameter equal to [3, 5, 10] and n is the total number of peaks recorded. By definition for $m = 1$ the total average on the whole pressure peaks is evaluated, increasing m the average concerns only the most energetic events, ($m = n$ implies that $p_{avg.1/mlargest} = p_1$ which is the highest pressure peak recorded). Figure 35 depicts the average on the $1/m$ largest peaks using m=[3, 5, 10]. When considering $m = 10$ the same conclusions drawn with $p_{avg.k.largest}$ with $k = 10$ are obtained. For the case **SW** we do not need even to change the pressure scale, due to the small number of recorded pressure peaks. This is not the case for the case **IW** and **DW** where the pressure scale is halved

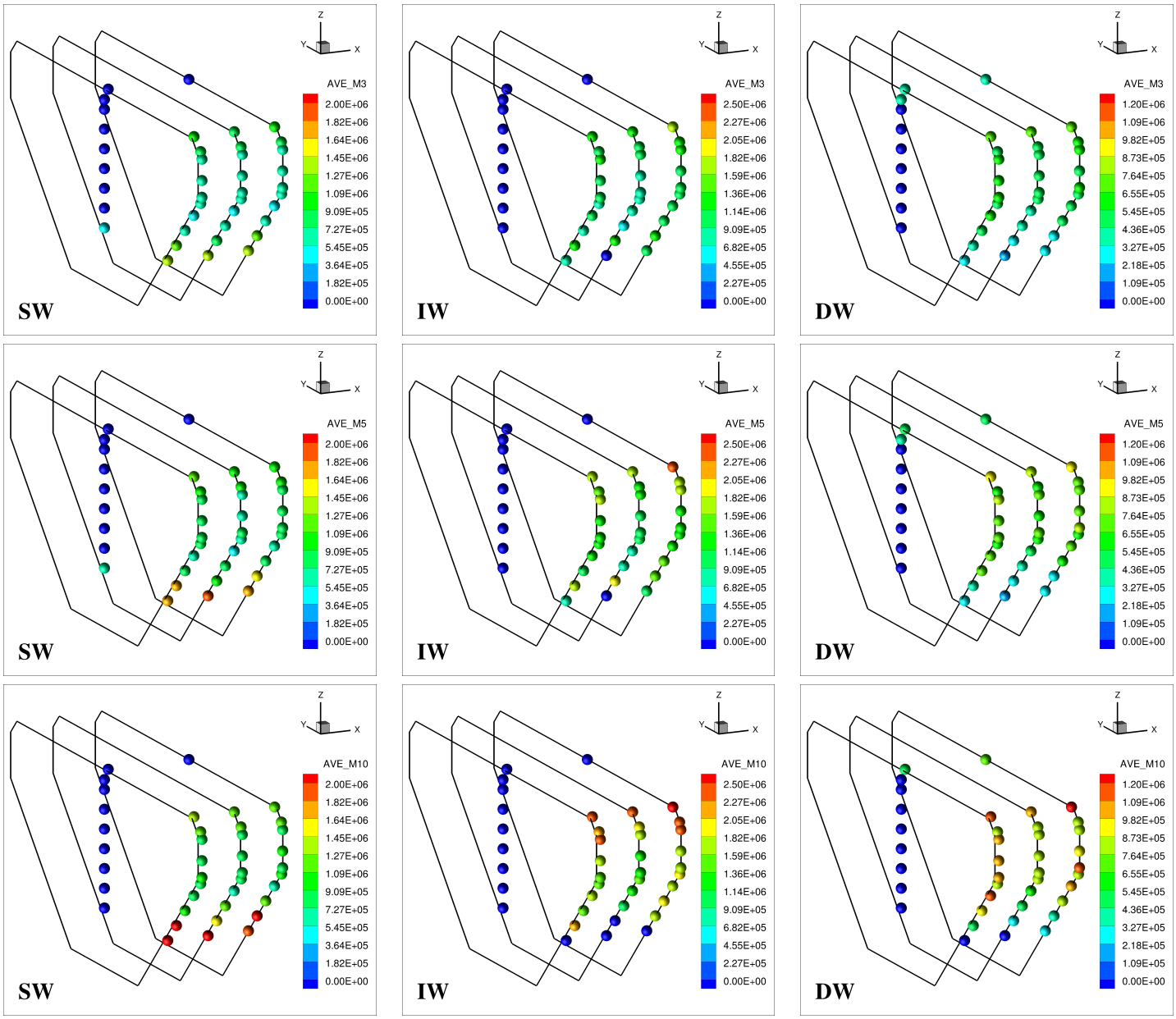

Figure 35: Average of 1/m largest pressure peaks with m=3 (top row), 5 (middle row), 10 (bottom row) for the case **SW** (left column), **IW** (middle column), **DW** (right column).

when passing from the $p_{avg.k.largest}$ to $p_{avg.1/mlargest}$.

Finally, for the sake of completeness, in tables 4, 5, 6 the same quantities plotted above are reported for all probes and for the three cases.

7. Conclusions

In the present work the numerical investigation of sloshing flows inside a ship LNG fuel tank was studied. Long time simulations, involving 3-hours real–time duration with realistic severe sea-state forcing, were performed using the parallel CFD software called SPH-Flow which ran for several weeks on a dedicated cluster. The adopted SPH method relies on a Riemann Solver for the calculation of the particle interactions which increases the stability of the scheme and allows for accurate predictions of the pressure during water impact stages.

Preliminary 2D sloshing simulations necessary for the selection of the optimal numerical parameters to be adopted in the 3D simulations have been performed. After this stage, 3D simulations with 3 different water depths have been launched. They have run for about six months on three dedicated blades, each of those equipped with 64 cores. After that a post-processing stage has been conducted in order to analyze the pressure time histories on 40 different probes. For the most critical events an analysis of the flow features has been also performed in order to better understand the obtained outcomes. The low filling case resulted to be by far the less critical condition. In the intermediate condition a slightly larger number of extreme events have been registered with respect to the deep filling condition.

The comparisons of the SPH outcomes with the experimental data shows that adopted SPH model is able to well predict the intensity of the pressure peaks while the numerical rise times are always overestimated.

The single phase SPH overestimates the time duration by an order of magnitude. The increase of the speed of sound combined with an increase of the spatial resolution may improve this aspect. However, on the contrary, this strategy could also increase the value of the pressure peaks since with finer resolutions a larger number of entrapped empty cavities could happen. By the way, due to the larger CPU costs, we cannot inspect the above analysis based on the increase of $H/\Delta r$ and larger speed of sound which leads to a large increase of the time iterations. On the other hand, again due to the constraints linked to the CPU costs, long-time simulations with a two phase model, as the one described in Hammani et al. (2020), still remain prohibitive nowadays. To overcome the above drawbacks, adaptive resolution algorithms (both in time and space) are needed. Since the number of particles adopted in the present study is not so large, the future implementation of the SPH-Flow code on graphics processing unit (GPU) (see *e.g.* Mokos et al. (2015)) may also allow a further improvement of the present analysis.

Declaration of competing interest

The authors declare that they have no known competing financial interests or personal relationships that could have appeared to influence the work reported in this paper.

CRediT authorship contribution statement

C. Pilloton: Conceptualization, Methodology, Investigation, Writing - original draft.
A. Bardazzi: Software, Data curation, Visualization, Validation.
A. Colagrossi: Supervision, Investigation, Writing - review & editing.
S. Marrone: Conceptualization, Software, Writing - review & editing, Resources.

Acknowledgements

The research activity was supported by the project SinSEOn "Sloshing SPH Environment for long-time Oscillation simulation", within the Memorandum of Understanding 2015-2018 between CNR-INM (formerly CNR-INSEAN) and the Hyundai Maritime Research Institute (HMRI) of Hyundai Heavy Industries Co. Ltd.

The work was partially supported by the SLOWD project which received funding from the European Union's Horizon 2020 research and innovation programme under grant agreement No 815044.

The SPH simulations performed under the present research were obtained using the SPH-Flow solver, software developed within a collaborative consortium composed of Ecole Centrale Nantes, NextFlow Software company and CNR-INM.

SW Test Case							
Probe	Peak Nb. #	K-Ave 3 (bar)	K-Ave 5 (bar)	K-Ave 10 (bar)	M-Ave 3 (bar)	M-Ave 5 (bar)	M-Ave 10 (bar)
BHD P1	8	4.7	3.9	0.0	5.2	6.3	0.0
BHD P2	1	0.0	0.0	0.0	0.0	0.0	0.0
BHD P3	0	0.0	0.0	0.0	0.0	0.0	0.0
BHD P4	0	0.0	0.0	0.0	0.0	0.0	0.0
BHD P5	0	0.0	0.0	0.0	0.0	0.0	0.0
BHD P6	0	0.0	0.0	0.0	0.0	0.0	0.0
BHD P7	0	0.0	0.0	0.0	0.0	0.0	0.0
BHD P8	0	0.0	0.0	0.0	0.0	0.0	0.0
LC P1	156	24.8	24.0	22.1	12.9	16.4	20.9
LC P2	110	25.1	24.0	22.6	12.5	17.1	22.2
LC P3	90	18.0	13.9	10.0	6.1	7.7	10.5
LC P4	137	14.5	11.6	8.9	5.3	6.4	8.1
LC P5	290	14.8	13.3	11.6	6.2	7.3	8.9
LC P6	132	23.3	22.3	21.0	14.1	18.2	20.3
LC P7	102	21.5	19.4	14.6	7.7	10.2	14.6
LC P8	66	18.1	13.5	9.2	6.1	8.0	12.1
LC P9	113	7.5	6.7	5.7	4.3	4.8	5.6
LC P10	270	10.5	10.2	9.4	5.9	6.8	7.9
LC P11	152	22.2	22.0	20.9	13.4	17.3	20.0
LC P12	123	23.7	23.1	21.5	11.6	16.4	20.9
LC P13	87	17.7	13.8	10.1	6.1	7.8	11.2
LC P14	138	9.9	8.8	7.2	4.6	5.5	6.8
LC P15	307	16.5	14.8	12.3	6.4	7.6	9.3
SW P1	559	15.5	14.8	13.2	6.4	7.7	9.2
SW P2	192	11.6	11.0	10.0	6.3	7.4	8.8
SW P3	223	14.9	12.8	10.6	6.4	7.4	8.8
SW P4	493	13.6	12.9	11.5	6.4	7.4	8.6
SW P5	186	10.3	9.8	9.1	5.8	7.0	8.2
SW P6	221	10.9	10.4	9.5	6.1	6.9	8.1
SW P7	564	18.1	16.1	13.3	6.3	7.5	9.1
SW P8	187	13.2	12.5	11.1	6.4	7.7	9.6
SW P9	239	14.0	12.9	11.2	6.4	7.5	9.2
T P1	0	0.0	0.0	0.0	0.0	0.0	0.0
T P2	251	19.0	17.3	15.3	9.8	11.2	13.0
T P3	245	14.1	13.6	12.8	9.0	10.1	11.5
T P4	257	15.9	15.2	14.1	9.7	10.9	12.4
T P5	1	0.0	0.0	0.0	0.0	0.0	0.0
UC P1	300	16.9	16.1	14.5	8.5	9.9	11.9
UC P2	279	15.4	14.8	13.6	8.6	9.8	11.3
UC P3	299	19.4	17.6	15.0	8.8	10.3	12.2

Table 4: Statistical outcome for the **SW** case (filling height 6.22 m).

IW Test Case							
Probe	Peak Nb. #	K-Ave 3 (bar)	K-Ave 5 (bar)	K-Ave 10 (bar)	M-Ave 3 (bar)	M-Ave 5 (bar)	M-Ave 10 (bar)
BHD P1	0	0.0	0.0	0.0	0.0	0.0	0.0
BHD P2	0	0.0	0.0	0.0	0.0	0.0	0.0
BHD P3	0	0.0	0.0	0.0	0.0	0.0	0.0
BHD P4	0	0.0	0.0	0.0	0.0	0.0	0.0
BHD P5	1	0.0	0.0	0.0	0.0	0.0	0.0
BHD P6	0	0.0	0.0	0.0	0.0	0.0	0.0
BHD P7	0	0.0	0.0	0.0	0.0	0.0	0.0
BHD P8	0	0.0	0.0	0.0	0.0	0.0	0.0
LC P1	5	6.6	5.3	0.0	9.0	9.0	0.0
LC P2	16	16.3	13.3	9.0	13.3	16.3	22.4
LC P3	66	18.1	15.3	11.8	8.4	10.6	14.5
LC P4	210	28.4	24.9	20.9	9.0	11.7	16.0
LC P5	397	28.3	26.5	23.3	8.4	11.0	15.0
LC P6	1	0.0	0.0	0.0	0.0	0.0	0.0
LC P7	6	10.4	7.7	0.0	13.1	19.6	0.0
LC P8	33	8.5	7.3	6.0	5.8	7.0	8.5
LC P9	124	16.9	14.9	12.0	7.1	8.8	11.2
LC P10	294	33.5	27.5	20.7	7.1	9.2	12.7
LC P11	7	9.1	8.2	0.0	9.3	9.7	0.0
LC P12	19	15.0	13.4	9.8	12.5	15.0	18.8
LC P13	58	22.8	18.6	14.5	11.1	14.0	18.6
LC P14	213	33.7	29.6	23.4	9.5	12.5	17.3
LC P15	424	43.6	39.0	31.7	9.8	13.0	18.2
SW P1	510	35.2	30.7	26.4	9.1	11.7	15.8
SW P2	333	32.4	31.0	26.7	9.6	12.6	17.1
SW P3	358	43.5	40.0	34.0	11.6	15.8	22.3
SW P4	364	26.6	22.8	18.9	7.3	9.1	12.1
SW P5	256	18.1	17.0	14.8	7.3	9.1	11.7
SW P6	275	33.0	29.6	23.9	9.1	12.0	16.4
SW P7	499	47.0	39.5	30.3	9.4	12.2	16.4
SW P8	364	39.7	32.7	25.7	9.6	12.1	16.0
SW P9	369	50.0	43.8	33.3	11.0	14.5	20.3
T P1	1	0.0	0.0	0.0	0.0	0.0	0.0
T P2	348	48.4	43.6	36.0	13.4	17.6	25.0
T P3	287	50.0	42.1	34.0	12.2	16.1	22.4
T P4	348	50.0	50.0	43.5	14.5	19.8	28.6
T P5	0	0.0	0.0	0.0	0.0	0.0	0.0
UC P1	372	50.0	42.4	31.9	10.7	14.0	19.2
UC P2	333	37.5	31.9	25.6	9.9	12.6	16.9
UC P3	410	50.0	44.9	35.5	11.8	15.4	21.1

Table 5: Statistical outcome for the **IW** case (filling height 12.44 m).

DW Test Case							
Probe	Peak Nb. #	K-Ave 3 (bar)	K-Ave 5 (bar)	K-Ave 10 (bar)	M-Ave 3 (bar)	M-Ave 5 (bar)	M-Ave 10 (bar)
BHD P1	0	0.0	0.0	0.0	0.0	0.0	0.0
BHD P2	0	0.0	0.0	0.0	0.0	0.0	0.0
BHD P3	1	0.0	0.0	0.0	0.0	0.0	0.0
BHD P4	0	0.0	0.0	0.0	0.0	0.0	0.0
BHD P5	0	0.0	0.0	0.0	0.0	0.0	0.0
BHD P6	0	0.0	0.0	0.0	0.0	0.0	0.0
BHD P7	1	0.0	0.0	0.0	0.0	0.0	0.0
BHD P8	7	3.3	2.8	0.0	3.7	3.9	0.0
LC P1	8	2.5	2.3	0.0	2.5	2.7	0.0
LC P2	31	4.7	4.1	3.4	3.4	3.9	4.7
LC P3	29	9.3	7.2	5.1	5.4	7.2	10.6
LC P4	81	18.1	14.5	10.3	6.1	8.0	11.5
LC P5	195	13.7	12.2	10.0	5.0	6.2	8.1
LC P6	7	2.1	2.0	0.0	2.2	2.2	0.0
LC P7	23	2.8	2.6	2.4	2.6	2.7	2.8
LC P8	26	4.4	3.8	3.2	3.4	3.8	4.8
LC P9	71	7.7	6.9	5.5	4.1	5.0	6.2
LC P10	162	12.8	11.5	9.5	4.7	5.9	7.9
LC P11	10	2.3	2.1	1.9	2.3	2.4	2.6
LC P12	41	4.0	3.6	3.1	2.9	3.2	3.8
LC P13	34	8.6	6.9	5.1	4.9	6.4	8.6
LC P14	69	15.3	12.4	8.9	5.7	7.7	11.4
LC P15	182	15.8	13.7	10.8	5.3	6.6	8.6
SW P1	350	26.8	21.8	17.5	6.0	7.6	10.4
SW P2	559	19.7	18.2	15.8	5.8	7.6	10.2
SW P3	1157	21.8	20.3	18.4	6.3	7.8	10.2
SW P4	294	13.7	12.6	11.1	5.1	6.4	8.1
SW P5	553	18.6	17.0	14.6	5.1	6.4	8.6
SW P6	821	14.6	14.5	13.8	5.4	6.7	8.5
SW P7	352	26.2	22.6	18.2	6.4	8.3	11.4
SW P8	557	21.2	18.7	16.0	5.5	7.0	9.4
SW P9	869	14.6	14.4	13.7	5.6	6.9	8.8
T P1	47	5.3	4.9	4.3	3.8	4.4	5.1
T P2	1297	40.5	32.6	25.6	7.2	9.0	11.7
T P3	1143	18.5	18.1	17.3	6.7	8.2	10.4
T P4	1258	41.0	36.8	28.7	7.5	9.4	12.2
T P5	52	6.9	6.6	5.1	4.3	5.1	6.6
UC P1	1136	15.9	15.4	14.5	5.3	6.5	8.3
UC P2	1055	16.2	15.1	13.8	5.2	6.4	8.2
UC P3	1278	21.3	19.1	16.4	5.7	7.0	8.8

Table 6: Statistical outcome for the **DW** case (filling height 18.66 m).

References

Abrahamsen, B. C., Faltinsen, O. M., 2013. Scaling of entrapped gas pocket slamming events at dissimilar euler number. Journal of Fluids and Structures 40, 246–256.

Ahn, Y., 2019. Data mining in sloshing model test database and application of neural network for test result prediction. Ph.D. thesis, Department of Naval Architecture and Ocean Engineering, Seoul National University.

Ahn, Y., Kim, Y., 2021. Data mining in sloshing experiment database and application of neural network for extreme load prediction. Marine Structures 80, 103074.

Ahn, Y., Kim, Y., Kim, S.-Y., 2019. Database of model-scale sloshing experiment for lng tank and application of artificial neural network for sloshing load prediction. Marine Structures 66, 66–82.

Antuono, M., Marrone, S., Di Mascio, A., Colagrossi, A., 2021. Smoothed particle hydrodynamics method from a large eddy simulation perspective. generalization to a quasi-lagrangian model. Physics of Fluids 33 (1), 015102.

Bouscasse, B., Antuono, M., Colagrossi, A., Lugni, C., 2013. Numerical and experimental investigation of nonlinear shallow water sloshing. International Journal of Nonlinear Sciences and Numerical Simulation 14 (2), 123–138.

Bouscasse, B., Colagrossi, A., Souto-Iglesias, A., Cercos-Pita, J., 2014a. Mechanical energy dissipation induced by sloshing and wave breaking in a fully coupled angular motion system. I. theoretical formulation and numerical investigation. Physics of Fluids 26 (3), 033103.

Bouscasse, B., Colagrossi, A., Souto-Iglesias, A., Cercos-Pita, J., 2014b. Mechanical energy dissipation induced by sloshing and wave breaking in a fully coupled angular motion system. II. experimental investigation. Physics of Fluids 26 (3), 033104.

Cao, X., Ming, F., Zhang, A., 2014. Sloshing in a rectangular tank based on SPH simulation. Applied Ocean Research 47, 241–254.

Chiron, L., De Leffe, M., Oger, G., Le Touzé, D., 2019. Fast and accurate SPH modelling of 3d complex wall boundaries in viscous and non viscous flows. Computer Physics Communications 234, 93–111.

Colagrossi, A., Bouscasse, B., Antuono, M., Marrone, S., 2012. Particle packing algorithm for SPH schemes. Computer Physics Communications 183 (2), 1641–1683.

Delorme, L., Colagrossi, A., Souto-Iglesias, A., Zamora-Rodriguez, R., Botia-Vera, E., 2009. A set of canonical problems in sloshing, part i: Pressure field in forced roll—comparison between experimental results and SPH. Ocean Engineering 36 (2), 168–178.

Di Mascio, A., Antuono, M., Colagrossi, A., Marrone, S., 2017. Smoothed particle hydrodynamics method from a large eddy simulation perspective. Physics of Fluids 29 (3), 035102.

Diebold, L., Baudin, E., 2014. Bureau veritas sloshing model tests & CFD calculations for isope sloshing benchmark. In: The Twenty-fourth International Ocean and Polar Engineering Conference. OnePetro.

DNV, 2006. Sloshing Analysis of LNG Membrane Tanks, Classification Notes, No. 30.9. Det Norske Veritas. Tech. rep.

Elahi, R., Passandideh-Fard, M., Javanshir, A., 2015. Simulation of liquid sloshing in 2d containers using the volume of fluid method. Ocean Engineering 96, 226–244.

Gómez-Goñi, J., Garrido-Mendoza, C., Cercós, J., González, L., 2013. Two phase analysis of sloshing in a rectangular container with volume of fluid (vof) methods. Ocean Engineering 73, 208–212.

Green, M. D., Peiró, J., 2018. Long duration SPH simulations of sloshing in tanks with a low fill ratio and high stretching. Computers & fluids 174, 179–199.

Hammani, I., Marrone, S., Colagrossi, A., Oger, G., Le Touzé, D., 2020. Detailed study on the extension of the δ-SPH model to multi-phase flow. Computer Methods in Applied Mechanics and Engineering 368, 113189.

Jean, P., Petit, H., 1998. Methane by sea—a history of french methane carrier techniques. France: Gaz Transport & Technigaz.

Kim, S.-Y., Kim, Y., Lee, J., 2017. Comparison of sloshing-induced pressure in different scale tanks. Ships and Offshore Structures 12 (2), 244–261.

Kuo, J., Campbell, R., Ding, Z., Hoie, S., Rinehart, A., Sandström, R., Yung, T., Greer, M., Danaczko, M., 2009. LNG tank sloshing assessment methodology-the new generation. In: The Nineteenth International Offshore and Polar Engineering Conference. OnePetro.

Lee, D., Kim, M., Kwon, S., Kim, J., Lee, Y., 2007. A parametric sensitivity study on lng tank sloshing loads by numerical simulations. Ocean Engineering 34 (1), 3–9.

Li, H., Li, J., Zong, Z., Chen, Z., 2014. Numerical studies on sloshing in rectangular tanks using a tree-based adaptive solver and experimental validation. Ocean engineering 82, 20–31.

Loysel, T., Chollet, S., Gervaise, E., Brosset, L., De Seze, P.-E., 2012. Results of the first sloshing model test benchmark. In: The Twenty-second International Offshore and Polar Engineering Conference. OnePetro.

Loysel, T., Gervaise, E., Moreau, S., Brosset, L., 2013. Results of the 2012-2013 sloshing model test benchmark. In: The Twenty-third International Offshore and Polar Engineering Conference. OnePetro.

Lugni, C., Brocchini, M., Faltinsen, O., 2010. Evolution of the air cavity during a depressurized wave impact. ii. the dynamic field. Physics of fluids 22 (5), 056102.

Lugni, C., Brocchini, M., Faltinsen, O. M., 2006. Wave impact loads: The role of the flip-through. Physics of Fluids 18 (12), 101–122.

Luo, M., Khayyer, A., Lin, P., 2021. Particle methods in ocean and coastal engineering, Applied Ocean Research 114, 102734.

Lyu, H., Sun, P., 2022. Further enhancement of the particle shifting technique: Towards better volume conservation and particle distribution in SPH simulations of violent free-surface flows. Applied Mathematical Modelling 101, 214–238.

Lyu, W., el Moctar, O., Potthoff, R., Neugebauer, J., 2017. Experimental and numerical investigation of sloshing using different free surface capturing methods. Applied Ocean Research 68, 307–324.

Malan, A., Jones, B., Malan, L., Wright, M., 2021. Accurate prediction of violent slosh loads via a weakly compressible vof formulation. In: The 31st International Ocean and Polar Engineering Conference. OnePetro.

Malenica, S., Sireta, F., Bigot, F., Wang, C., Chen, X., 05 2009. Some aspects of hydro-structure coupling for combined action of seakeeping and sloshing. In: International Conference on Offshore Mechanics and Arctic Engineering. Vol. Volume 6: Materials Technology; C.C. Mei Symposium on Wave Mechanics and Hydrodynamics; Offshore Measurement and Data Interpretation. pp. 461–467.

Marrone, S., Colagrossi, A., Di Mascio, A., Le Touzé, D., 2015. Prediction of energy losses in water impacts using incompressible and weakly compressible models. Journal of Fluids and Structures 54, 802–822.

Marrone, S., Colagrossi, A., Di Mascio, A., Le Touzé, D., 2016. Analysis of free-surface flows through energy considerations: Single-phase versus two-phase modeling. Physical Review E 93 (5), 053113.

Marrone, S., Colagrossi, A., Park, J., Campana, E., 2017. Challenges on the numerical prediction of slamming loads on lng tank insulation panels. Ocean Engineering 141, 512–530.

Maruzewski, P., Touzé, D. L., Oger, G., Avellan, F., 2010. SPH high-performance computing simulations of rigid solids impacting the free-surface of water. Journal of Hydraulic Research 48 (S1), 126–134.

Meringolo, D., Colagrossi, A., Marrone, S., Aristodemo, F., 2017. On the filtering of acoustic components in weakly-compressible SPH simulations. Journal of Fluids and Structures 70, 1–23.

Moirod, L. D., Baudin, E., Gazzola, T., et al., 2011. Experimental and numerical investigations of internal global forces for violent irregular excitations in lngc prismatic tanks. In: The Twenty-first International Offshore and Polar Engineering Conference. OnePetro.

Mokos, A., Rogers, B.D., Stansby, P.K., Domínguez, J.M., 2015. Multi-phase SPH modelling of violent hydrodynamics on GPUs. Computer Physics Communications 196, 304–316.

Monaghan, J. J., 1992. Smoothed particle hydrodynamics. Annual review of astronomy and astrophysics 30 (1), 543–574.

Monaghan, J. J., 2012. Smoothed particle hydrodynamics and its diverse applications. Annual Review of Fluid Mechanics 44, 323–346.

Oger, G., Le Touzé, D., Guibert, D., de Leffe, M., Biddiscombe, J., Soumagne, J., Piccinali, J.-G., 2016. On distributed memory MPI-based parallelization of SPH codes in massive HPC context. Computer Physics Communications 200, 1–14.

Parshikov, A. N., Medin, S. A., 2002. Smoothed particle hydrodynamics using interparticle contact algorithms. Journal of computational physics 180 (1), 358–382.

Peregrine, D., 2003. Water-wave impact on walls. Annual Review of Fluid Mechanics 35 (1), 23–43.

Shadloo, M. S., Oger, G., Le Touzé, D., 2016. Smoothed particle hydrodynamics method for fluid flows, towards industrial applications: Motivations, current state, and challenges. Computers & Fluids 136, 11–34.

Shao, J., Li, H., Liu, G., Liu, M., 2012. An improved sph method for modeling liquid sloshing dynamics. Computers & Structures 100, 18–26.

Smagorinsky, J., 1963. General circulation experiments with the primitive equations: I. the basic experiment. Monthly weather review 91 (3), 99–164.

Violeau, D., Rogers, B. D., 2016. Smoothed particle hydrodynamics (SPH) for free-surface flows: past, present and future. Journal of Hydraulic Research 54 (1), 1–26.

Wei, Z., Ruan, S., Chen, X., Luo, S., Yue, Q., 2014. An experimental investigation of liquid sloshing impact load in a large-scaled prismatic tank. In: The Twenty-fourth International Ocean and Polar Engineering Conference. OnePetro.

You, Y., Khayyer, A., Zheng, X., Gotoh, H., Ma, Q., 2021. Enhancement of δ-SPH for ocean engineering applications through incorporation of a background mesh scheme. Applied Ocean Research 110, 102508.